

Bifunctional TiO₂ – cellulose based nanocomposites for synergistic adsorptive-photocatalytic removal of methyl orange: Response modelling and optimization

Marwa Ezzine, Ahmed S. El-Shafie, Khaled M. Youssef, Marwa El-Azazy

Item type

Journal Contribution

Terms of use

This work is licensed under a [CC BY 4.0](#) license

This version is available at

[https://manara.qnl.qa/articles/journal_contribution/Bifunctional_TiO_sub_2_sub_cellulose_based_nanocomposites_for_synergistic photocatalytic_removal_of_methyl_orange_Response_modelling_and_optimization/28546619/1](https://manara.qnl.qa/articles/journal_contribution/Bifunctional_TiO_sub_2_sub_cellulose_based_nanocomposites_for_synergistic_photocatalytic_removal_of_methyl_orange_Response_modelling_and_optimization/28546619/1)

Access the item on Manara for more information about usage details and recommended citation.

Posted on Manara – Qatar Research Repository on

2025-03-19



Bifunctional TiO₂ – cellulose based nanocomposites for synergistic adsorptive-photocatalytic removal of methyl orange: Response modelling and optimization

Marwa Ezzine^a, Ahmed S. El-Shafie^b, Khaled M. Youssef^a, Marwa El-Azazy^{b,*}

^a Materials Science and Technology Graduate Program, Department of Physics and Materials Science, College of Arts and Sciences, Qatar University, Doha 2713, Qatar

^b Department of Chemistry and Earth Sciences, College of Arts and Sciences, Qatar University, Doha 2713, Qatar

ARTICLE INFO

Keywords:

Cellulose-like structures
Titanium oxide
Synergistic adsorption-photocatalysis

ABSTRACT

Removal of azo dyes from aquatic environments represents a global challenge. Herein, by utilizing the waste of mandarin peels as a cellulose source (MP500), a bifunctional adsorbent-photocatalyst, TiO₂@MP500, has been prepared via a one-pot hydrothermal synthesis. Taking advantage of this dual role, remediation of methyl orange (MO) has been successfully addressed. Characterization tools corroborated the anchoring of TiO₂ and the successful synthesis of TiO₂@MP500. SEM/EDX/TEM analyses confirmed the formation of TiO₂ nanoparticles on the carbonaceous surface. A substantial increase in the BET surface area following TiO₂ impregnation was perceived (184.61 m²/g in the case of 3 %TiO₂@MP500). Similarly, the thermal stability of the developed composite was notably improved as reflected by the thermogravimetric analysis. XRD analysis corroborated the existence of carbonaceous layer with anatase phase TiO₂. Optimization of the adsorbent-photocatalyst performance was approached using the Box-Behnken design. Five factors were premeditated, pH of the MO solution, adsorbent dose, reaction time, the concentration of TiO₂, and [MO]. A maximum sorption capacity of 104.2 mg/g was reckoned, with a pseudo-second-order isotherm. Furthermore, the 3 %TiO₂@MP500 achieved a decolorization efficiency of 98.87 % in ~30 min. The 3 %TiO₂@MP500 nanocomposite was effectively revived and could be exploited for 6 cycles, bolstering a decolorization efficiency of 90.91 %.

1. Introduction

Availability of clean water has streamed as a major concern that escalates day after day. With human life's advancements over the past few decades, a concomitant improvement in living standards has been glimpsed. Such an improvement has gone parallel with proportionate progress in the textile industries and an increased consumption of dyes and colorants. The textile industry has been held responsible for ~15–20 % of dyes polluted wastewater worldwide [1–4]. With ~10,000 dyes being synthesized annually, around 500,000 tons are dumped into the environment [5,6]. Among the synthetic textile dyes, two-thirds are azo dyes, thanks to their compelling tanning properties, fast colors, and high aqueous solubility [7–9].

Methyl orange (MO) is extensively used for research purposes, mainly as an acid-base indicator. Moreover, MO is highly pigmented with a high tinturing ability and therefore commonly used for tanning, leather, paper, and pulp industries. The chemical structure and the 3D

model of MO, together with the physicochemical and toxicity data, are displayed in Table S1. Yet, with all these fascinating attributes, the complex structure of MO hampers its degradation, and the degradation byproducts are well-known for being toxic for both humans and aquatic organisms [4–6,10].

A number of techniques have been elaborated for the remediation of the azo dyes polluted wastewater, for instance, coagulation-flocculation [11], membrane filtration [12], microbial degradation [13], adsorption [14,15], photocatalysis [16,17], and electrocatalytic degradation [18]. While many of the reported techniques, especially adsorption, are sustainable and simple to operate, the comprehensive elimination of the dye cannot be realized. Moreover, the concentration of the dye on the adsorbent surface increases the risk of leaching and the potential of secondary pollution, which requires further treatments [19,20]. Nevertheless, photocatalysis can completely irradiate the target dye, but the high energy consumption and low selectivity are major concerns [21]. Moreover, the sluggish kinetics of dye degradation and 'electron-

* Corresponding author.

E-mail address: marwasaid@qu.edu.qa (M. El-Azazy).

<https://doi.org/10.1016/j.ijbiomac.2025.141753>

Received 11 September 2024; Received in revised form 19 February 2025; Accepted 3 March 2025

Available online 4 March 2025

0141-8130/© 2025 The Authors. Published by Elsevier B.V. This is an open access article under the CC BY license (<http://creativecommons.org/licenses/by/4.0/>).

hole' pair recombination can impede the effectiveness of photocatalysis in wastewater with organic loads.

The synchronized application of adsorption and photocatalysis has emerged as a revolutionary hybrid that coalesces the pluses of both techniques. In this combination, adsorbent plays a role by acting as a support material for the photocatalyst, allowing the concentration of the dye on the adsorbent surface and facilitating the dye exposure to the photocatalyst effect. Moreover, having the adsorbent backbone prevents the agglomeration of the photocatalyst nanoparticles [22,23]. To that end, this approach does not only make the removal process more competent and cost-effective but environmentally friendly as well by precluding the expected leaching into the environment while assisting the reusability of the adsorbent-photocatalyst materials [24].

The choice of the adsorbent backbone is therefore crucial to both allowing reusability and preventing secondary pollution via leaching. Activated carbons, graphene, layered double hydroxides, bentonite clay, and chitosan are the materials that have been reported as substrates for the immobilization of photocatalysts [25–29]. Compared to these commonly applied substrates, biochar – a carbonaceous material obtained via pyrolysis of biomasses – is a more economical and eco-friendly choice [30]. Implementing biochar as a substrate could improve the photocatalytic performance of biochar-based catalysts by increasing their ability to adsorb more dye molecules and minimize the aggregation of photocatalyst nanoparticles [10,19].

Cellulose-based materials such as fruit peels are among the biodegradable polymers that have been extensively used as an effective source of biochar [31]. The main objective of the current investigation is to develop a model bifunctional adsorbent-photocatalyst via recycling of the biochar of mandarin peels—a copiously available waste material rich in pectin, cellulose, and hemicellulose into an adsorbent [32–34]. In this regard, a semiconductor metal oxide, titanium oxide (TiO₂) – anatase form, was anchored on the surface via a simple hydrothermal approach and with the aid of a surfactant to control the particle size. The porous adsorbent-photocatalyst composite was used to remove the azo dye; methyl orange (MO), via a synergetic adsorption-photocatalysis mechanism. The performance of the bifunctional adsorbent-photocatalyst was explored in light of the findings of the Box-Behnken (BB) design. Maximum performance towards MO removal with the minimum possible consumption of resources was guaranteed by using the optimum variable settings provided by the BB design [35,36]. The influence of calcination on the stability of the developed photocatalyst was figured out. The decolorization mechanism was analyzed considering the findings of BB design, characterization, and the adsorption equilibrium and kinetics. Our research, therefore, marks a significant step forward in harnessing the potential of the integration of adsorption-photocatalysis via an eco-friendly scheme for environmental remediation.

2. Experimental

2.1. Materials

Mandarin peels (MP) were obtained as home post-consumption waste. All chemicals were of high purity, sourced from Sigma-Aldrich (USA), and were used with no extra treatment steps. All experiments were conducted using ultrapure deionized water with a resistivity of 18.2 MΩ·cm at room temperature and a total organic carbon content of ≤5 ppb, obtained from the Millipore-Q system. For adsorption studies – batch mode, a stock aqueous solution of 100 ppm of MO (BDH Chemicals Ltd) was prepared. A series of additional dilutions were prepared in deionized water.

2.2. Preparation of mandarin peels (MP)-based sorbents

Mandarin fruits were first peeled, cleaned 10 times with tap water, and then 10 more times with deionized water to remove any unclean residues. Clean peels were left in the oven at 70 °C for 4 days. The dry

peels were powdered in the blender and then sifted through a 125 mm sieve. Afterward, the powder was burned for 1 h at 500 °C in a sealed crucible and placed in the furnace (Thermolyne™, USA). The product of this carbonization process was sealed in vials and marked as MP500.

2.3. Synthesis of TiO₂@MP500 binary composites

Loading of TiO₂ nanoparticles onto the surface of MP500 was accomplished using the hydrothermal synthesis [10]. Particle size was regulated using oleylamine solution as a surfactant. In this regard, a 100 mL of 0.1 M surfactant solution was prepared by dissolving 3.2 mL oleylamine in 2-propanol. The oleylamine solution was then mixed with 300 mL of deionized water. The resulting solution was mixed with 10 g of MP500 and different volumes of 0.09 M TiCl₄ solution (34, 68, and 102 mL) in separate batches, followed by heating at 80 °C and stirring at 500 rpm for a duration of 1 h. The pH of the resultant solution was attuned to ~1.8 using NH₃ solution (26 %). The prepared sample was agitated for 2 h at 80 °C. Following this step, a 26 % NH₃ solution was used to increase the mixture pH to ~8. The prepared sample was agitated for 20 h at ambient temperature. The product was separated by centrifugation (ThermoFisher Scientific, USA) using a rotation speed of 4000 rpm for 10 min, cleaned 5 times with 30 mL deionized water, and then 5 times with 15 mL of ethanol. The resulting product was oven-dried overnight at 80 °C. The product was then calcinated in the furnace at 500 °C for 30 min. The final product has been labelled as TiO₂@MP500.

2.4. Characterization and measurements

The prepared samples were fully characterized using a set of techniques, including SEM/EDS, TEM, FTIR, TGA, BET and XRD analyses. Instrumental specifications are detailed in Text S1. The point of zero charges (pH_{PZC}) of MP500 and TiO₂@MP500 were determined using NaCl (0.01 M) aqueous solution and following the reported procedure in the literature [37]. Additionally, the pH of the dye solution was regulated using 0.1 M solutions of NaOH and HCl.

2.5. MO batch adsorption procedures

BB design was utilized to inspect the effect of five factors, including pH, adsorbent dose, reaction time, %TiO₂ loaded on the biochar, and the MO concentration on the removal efficiency (%R) of MO onto MP500 and TiO₂@MP500, Table 1. Eq. (1) was operated to work out the %R.

$$\%R = 100 \times \frac{C_0 - C_e}{C_0} \quad (1)$$

Where C₀ represents the initial concentration of MO (ppm), C_e corresponds to the equilibrium concentration of MO (ppm).

Table S2 details the experimental setup, which included 46 runs over two blocks. Each run has adhered to the specified conditions in Table S2, and the resulting %R was computed. In a typical experiment, the mass of the adsorbent was taken as illustrated for each run, and [MO] was then added. Subsequently, an adjusted pH (buffer) solution was added until the total volume = 13 mL. The samples were then shaken in an automatic shaker at a constant rotation speed of 160 rpm for the reaction

Table 1
BB design: Dependent and independent variables.

Variables	−1	0	+1
(A) pH (pH unit)	2	6	10
(B) Adsorbent dose of TiO ₂	10	65	120
(C) Reaction time, RT (min)	10	80	150
(D) %TiO ₂ added to Biochar	1 %	2 %	3 %
(E) MO concentration, [MO] (ppm)	10	35	60
Dependent variable	Removal percentage, %R		

time specified in Table S2. The obtained samples were then filtered using a 0.45 μm syringe filter and the absorbance was recorded at λ_{max} 462 nm for samples at pH 6 and pH 10 and at λ_{max} 502 nm for the sample prepared at pH 2.

For optimizing the assessed response, the d value (individual variables desirability function) available in Minitab® was utilized. Besides, the results obtained from the analysis of variance (ANOVA) were compared with the results of the other quality tools. Regression analyses were performed, examining metrics like R^2 , adjusted R^2 ($R^2\text{-adj}$), and the predicted R^2 ($R^2\text{-pred}$) to evaluate the models' linearity and predictive efficiency. Predicted values are shown in Table S2.

2.6. Equilibrium and kinetic investigations

Adsorption of MO onto 3 %TiO₂@MP500 was studied using four equilibrium models, and the samples were prepared using an initial MO stock solution, 500-ppm. Firstly 0.1000 \pm 0.0001 g of 3 %TiO₂@MP500 was added in eleven (13 mL) centrifuge tubes. This was followed by the addition of MO with different dilutions within the range of 2–250 ppm, and the pH was precisely controlled to 6.00 \pm 0.01. These tubes were then shaken at 160 rpm in an automatic shaker for 24 h. The mixtures were filtered using a 0.45 μm syringe filter, and the absorbances of the resulting solutions were recorded.

To study adsorption kinetics, 0.500 \pm 0.001 g of 3 %TiO₂@MP500 was mixed with 200 mL of a 100-ppm MO solution. The solution pH was tuned to 6.00 \pm 0.01. The prepared solution was then agitated at 750 rpm at ambient temperature. Over a span of 120 min, 10 mL samples were periodically taken, filtered through a 0.45 μm syringe filter, and their absorbance was recorded.

2.7. Photocatalytic activity of TiO₂@MP500: reaction kinetics

An experiment was executed to evaluate the photocatalytic performance of TiO₂@MP500. Initially, 0.500 \pm 0.001 g of the adsorbent, incorporating 1 %, 2 %, and 3 % TiO₂, was combined with a volume of 150 mL of a 100-ppm MO solution, adjusting the pH to 6.00 \pm 0.01. The mixture was then agitated continuously at 650 rpm under the illumination of a UV lamp emitting short-wavelength radiation at 254 nm. Throughout the irradiation period, 10 mL samples were systematically taken at constant intervals and filtered using a 0.45 μm syringe filter over 120 min. The absorbance of these filtrates was measured. The same procedures were repeated with the direct photolysis of MO solution (without adsorbent) and similarly following the addition of 0.500 \pm 0.001 g of MP500. Pure TiO₂ (without a biochar-support) was similarly (0.500 \pm 0.001 g) applied for the decolorization of MO. The data obtained from the experiment were processed through second-order polynomial fitting to determine the photocatalyst's decolorization efficiency (%DE) towards MO, calculated according to Eq. (2).

$$\%DE = 100 \times \frac{C_o - C_t}{C_o} \quad (2)$$

2.8. Regeneration of the adsorbent 3 %TiO₂@MP500

To assess the reusability of the adsorbent, 2.000 \pm 0.001 g of 3 %TiO₂@MP500 was initially saturated with 150 mL of a 100-ppm solution containing MO for 2 h, followed by filtration using an ashless Whatman filter paper (size 42). MO-loaded 3 %TiO₂@MP500 was rinsed 5 times with 10 mL of deionized water to remove residual non-adsorbed MO and dried at 80 °C for 24 h. The elution study utilized five different eluents, 0.1 M of HCl, H₂SO₄, and Na₂CO₃, 10 % ethanol, and deionized (DI) water. For the desorption tests, 0.1000 \pm 0.0001 g of the adsorbent laden with MO was treated with 10 mL of each eluent and agitated for 60 min before being filtered using an ashless Whatman filter paper (size 42). These desorption tests were replicated thrice, with the mean desorbed amount noted and variations depicted through error bars.

In the recovery experiment, 0.1 M HCl was utilized for MO elution from MO-loaded 3 %TiO₂@MP500. A mass of 0.5000 \pm 0.0001 g of 3 %TiO₂@MP500 was immersed in 50 mL of a 50-ppm dye solution (pH 6.0 \pm 0.2) for 30 min, then the mixture was filtered using an ashless Whatman filter paper (size 42), and absorbance of the produced filtrate was recorded. After being eluted with 0.1 M HCl, the adsorbent was dried at 80 °C for an hour before reuse in subsequent MO adsorption processes. This procedure was repeated six times, with the adsorption efficiency (%R) calculated after each cycle.

3. Results and discussion

3.1. Characterization

3.1.1. Morphology analysis using SEM, EDX, and TEM techniques

The SEM analysis, presented in Fig. 1, was used to investigate the microstructural attributes and the morphology of MP500 and the TiO₂@MP500 nanocomposites. Fig. 1(a, b) showcases the morphology of MP500, highlighting a plane surface that is free from particles. MP500 exhibits a layered pore configuration with finely granulated particles and small intra-pores. Conversely, Fig. 1(c, d) displays the SEM image of the 1 %TiO₂@MP500 nanocomposite, revealing the presence of tiny particles of TiO₂ that cover small areas on the surface of MP500, and the presence of MP500 as a support for these fine particles. Furthermore, the SEM images of the 2 %TiO₂@MP500 nanocomposite, Fig. 1(e, f), show also the presence of TiO₂ nanoparticles. However, the nanoparticles have accumulated in certain areas on the MP500 substrate and showed the presence of MP500 carbonaceous layers. Furthermore, Fig. 1(g, h) shows the micrographs of the 3 %TiO₂@MP500 nanocomposite, which reveal a dense layer of uniformly arranged blocks of TiO₂ nanoparticles covering almost all the surface of MP500.

The elemental structure of MP500 and the TiO₂@MP500 nanocomposites were examined using EDX, Fig. 2. The primary constituents of the pristine MP500 were identified as carbon and oxygen, along with smaller amounts of potassium, calcium, and magnesium, Fig. 2a. The obtained data were further confirmed using mapping images of MP500 for carbon, oxygen, and potassium, as shown in Fig. 2b, c, and d, respectively.

For the 1 %TiO₂@MP500 nanocomposite, analysis showed the presence of the same elements previously shown in the MP500 sample, in addition to chloride (1.47 %), and titanium (0.88 %), Fig. 2e. The incidence of chloride in the TiO₂-impregnated sample could have originated from using titanium chloride solution during the synthesis of TiO₂. The findings of the EDX analysis were confirmed using mapping images. The resulting data showed the presence of carbon, Fig. 2f, oxygen, Fig. 2g, and titanium, Fig. 2h, and confirmed the presence of titanium.

Similarly, the EDX analysis of 2 %TiO₂@MP500 showed the presence of carbon, oxygen, and 1.69 % titanium, Fig. 2i, and it was then confirmed using the mapping images, Fig. 2j-l. The EDX analysis of 3 %TiO₂@MP500 revealed the presence of titanium (3.36 %), Fig. 2m, and was further affirmed by mapping, Fig. 2n-p. The mapping analysis, Fig. 2p, shows that titanium covers all the surface of the carbonaceous backbone in alignment with the SEM findings. These results verify the successful impregnation of the biochar with TiO₂.

Fig. 3 showcases the TEM images of the MP500 and TiO₂@MP500 nanocomposites. The image obtained for pristine MP500, Fig. 3a, shows the presence of a carbonaceous layer of biochar with a plain surface, in agreement with the SEM findings. The bright-field TEM images for 1 %TiO₂@MP500, Fig. 3b and c, show the presence of TiO₂ nanoparticles on the surface. The particle size distribution, Fig. 3d, reveals that the TiO₂ particle size was 13.87 \pm 3.11 nm. The obtained images for 2 %TiO₂@MP500, Fig. 3e-g, show the presence of TiO₂ nanoparticles with particle size distribution of 3.01 \pm 0.52 nm, Fig. 3h. The small standard deviation calculated for the 155 particles denotes the formation of uniform TiO₂ nanoparticles on the biochar surface. For the 3 %

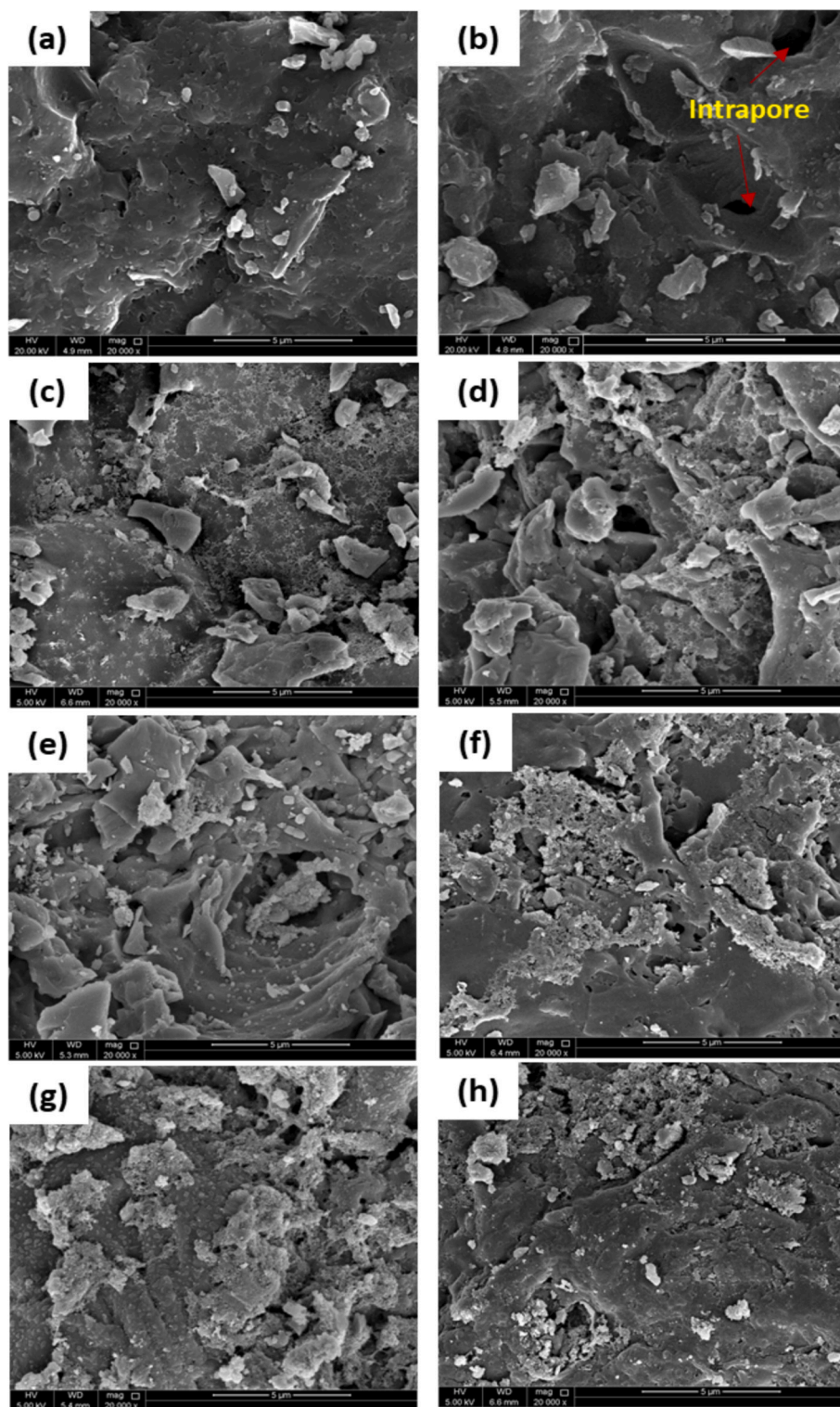


Fig. 1. SEM micrographs with magnification of 20,000 \times of MP500 (a, b), 1 %TiO₂@MP500 (c, d), 2 %TiO₂@MP500 (e, f), and 3 %TiO₂@MP500 (g, h).

TiO₂@MP500, the TEM images in Fig. 3i-k indicate the presence of TiO₂ nanoparticles that cover the surface of the biochar. Fig. 3j shows the bright field image of the TiO₂ nanoparticles and the corresponding selected area electron diffraction pattern (inset of Fig. 3j). The particle size distribution (Fig. 3l) indicates the presence of 2.74 ± 0.43 nm nanoparticles, revealing a smaller particle size and lower standard deviation. The high-resolution TEM image in Fig. 3k shows the lattice imaging of the TiO₂ nanoparticles with the corresponding (011) lattice

planes.

3.1.2. Analysis of specific surface area

Fig. 4 and Table S3 display the analysis results for the surface area and pore size of the prepared samples. Fig. 4a shows a notable increase in the multi-point BET surface area of the sample following the TiO₂ impregnation. The surface area was noted to increase from 2.19 m²/g for MP500 to 54.69 m²/g, 111.87 m²/g, and 184.61 m²/g for the 1 %, 2 %, and 3 % TiO₂ impregnation, respectively.

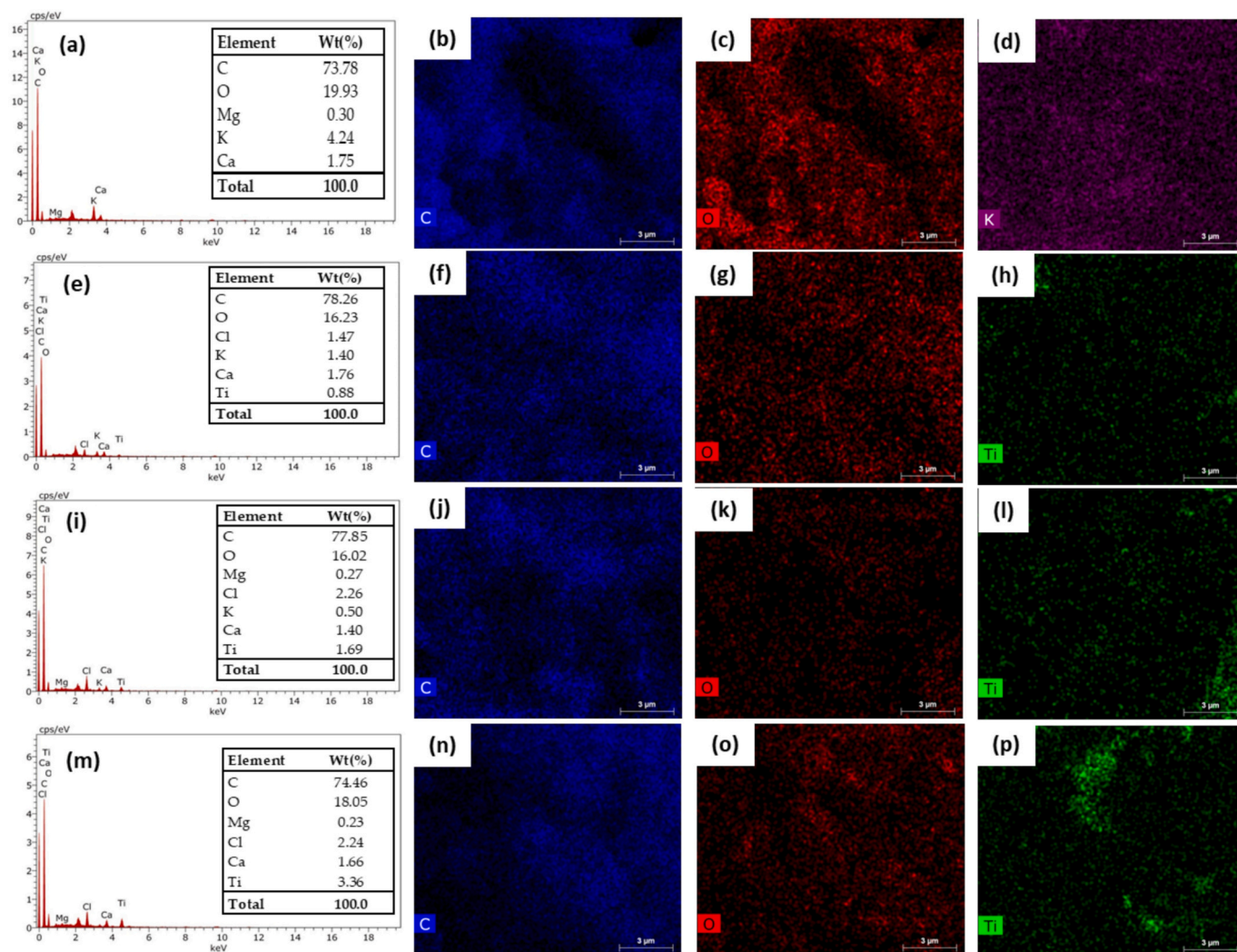


Fig. 2. EDX and mapping of MP500 (a–d), 1 %TiO₂@MP500 (e – h), 2 %TiO₂@MP500 (i – l), and 3 %TiO₂@MP500 (m – p).

and 3 %TiO₂@MP500, respectively. This significant increase in surface area has resulted from the distribution of TiO₂ nanoparticles on the surface of the nanocomposite, fostering the surface area affecting the adsorption efficiency and the photocatalytic decolourization towards the adsorbed MO molecules.

The mesoporosity of the surface structure of all prepared samples was proven by the pore size distribution, Fig. 4b, which revealed the presence of pores with a diameter of 2–50 nm. Table S3 illustrates that the average pore radius decreased from 162.7 Å for MP500 to 20.4 Å for 3 %TiO₂@MP500, a change resulting from the deposition of the TiO₂ nanoparticles inside the pore, resulting in a lower pore radius.

3.1.3. Assessment of thermal stability of the prepared adsorbents

Thermal stability plays a critical role in determining the suitability of materials for manufacturing and use under different environmental conditions. Thermogravimetric analysis (TGA) has been utilized to assess the thermal stability and decomposition temperatures of MP500 before and after impregnation with different concentrations of TiO₂. According to the TGA curve shown in Fig. 5, all samples have two distinct phases of weight loss. For the biochar sample, MP500, the initial phase, occurring between 50 and 150 °C, results in a 5.53 % weight loss that could be attributed to the removal of the adsorbed surface water [38,39]. The second phase, between 300 and 900 °C, reveals a 33.33 % loss in mass, likely due to the dehydration and the breakdown of the MP500 polymeric material and the formation of a carbonaceous

material [40]. The data also shows that 61.14 % of the MP500 mass remained after heating the sample to 900 °C.

On the other hand, the TiO₂ nanoparticles-impregnated sample reveals higher thermal stability where in the first stage a weight loss of 8.82 %, 8.13 %, and 7.64 % for 1, 2, and 3 %TiO₂@MP500, correspondingly, was observed and could be resulting from the loss of physical water adsorbed on the surface of the nanocomposite. The second phase showed losses of 29.03 %, 27.48 %, and 25.98 %, respectively, resulting from the carbonization of the polymeric material. It also shows a broad endothermic DTA peak, which illustrates the degradation of hemicellulose and the cellulose present in the MP500 biomass [40]. The obtained data show that the residual weight (%) of the impregnated samples after heating to 900 °C were 62.15 %, 64.39 %, and 66.38 % for 1 %, 2 %, and 3 %TiO₂@MP500, respectively, revealing that impregnation with TiO₂ enhances the thermal stability of the developed composite, thus the thermal stability increases as the concentration of loaded TiO₂ nanoparticles increases.

3.1.4. XRD analysis

The crystallinity of the MP500 and TiO₂@MP500 nanocomposites was examined using X-ray diffraction (XRD) analysis, Fig. 6. The XRD spectrum indicates that the samples possess well-defined crystallinity, as evidenced by the increased intensity of the observed peaks. The XRD pattern for the MP500 exhibits a broad peak ranging from 2θ: 20° to 28°. This peak shows the manifestation of the graphitic carbon amidst the

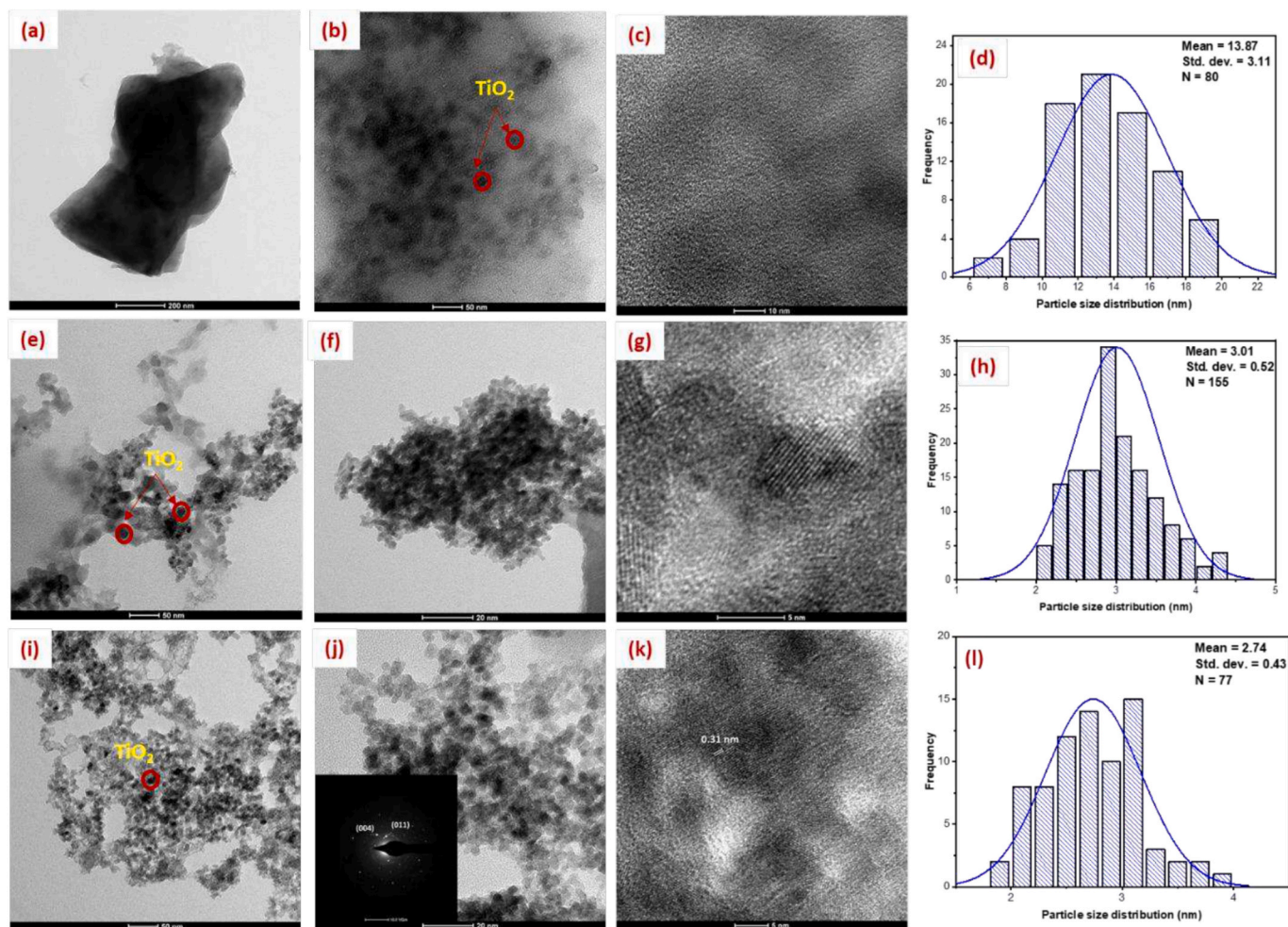


Fig. 3. TEM image of MP500 (a), 1 %TiO₂@MP500 (b, c), 2 %TiO₂@MP500 (e – g), and 3 %TiO₂@MP500 (i – k) and particle size distribution of 1 %TiO₂@MP500 (d), 2 %TiO₂@MP500 (h), and 3 %TiO₂@MP500 (l).

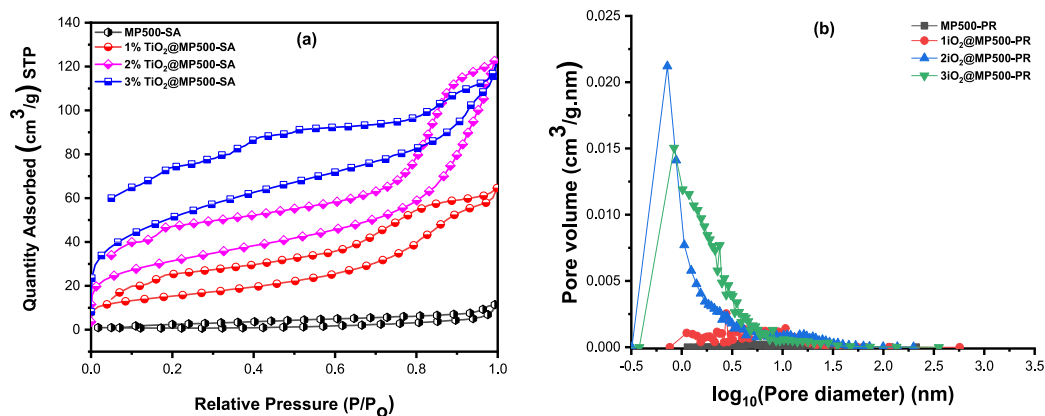


Fig. 4. (a) Measured surface area and (b) pore volume for MP500, 1 %TiO₂@MP500, 2 %TiO₂@MP500, and 3 %TiO₂@MP500.

amorphous carbon, which is typical of biochar (ICSD:426931) [41]. This broad peak persists in the spectra for TiO₂@MP500 samples, suggesting the presence of the carbonaceous layer alongside TiO₂ nanoparticles [42,43]. The XRD patterns for TiO₂ in the as-prepared samples 1 %TiO₂, 2 %TiO₂, and 3 %TiO₂@MP500 reveal peaks at 2θ values of 28.47°, 32.81°, 40.73°, and 50.44°, attributed to the anatase phase of TiO₂ and matching the hkl indices of (011), (004), (200), and (105), correspondingly (ICSD: 01–089) [44,45]. Identifying these distinctive planes

corroborates the presence of the anatase TiO₂ nanoparticles. Additionally, the XRD patterns of the TiO₂@MP500 demonstrate that the composite is of high purity with clearly defined diffraction peaks.

3.1.5. Raman analysis

Raman spectra of the as-prepared samples MP500 and 1, 2, and 3 % TiO₂@MP500 are shown in Fig. S1a. Obtained spectra show the presence of diffraction peaks at 1359 cm⁻¹ (D-peak) and 1589 cm⁻¹ (G-

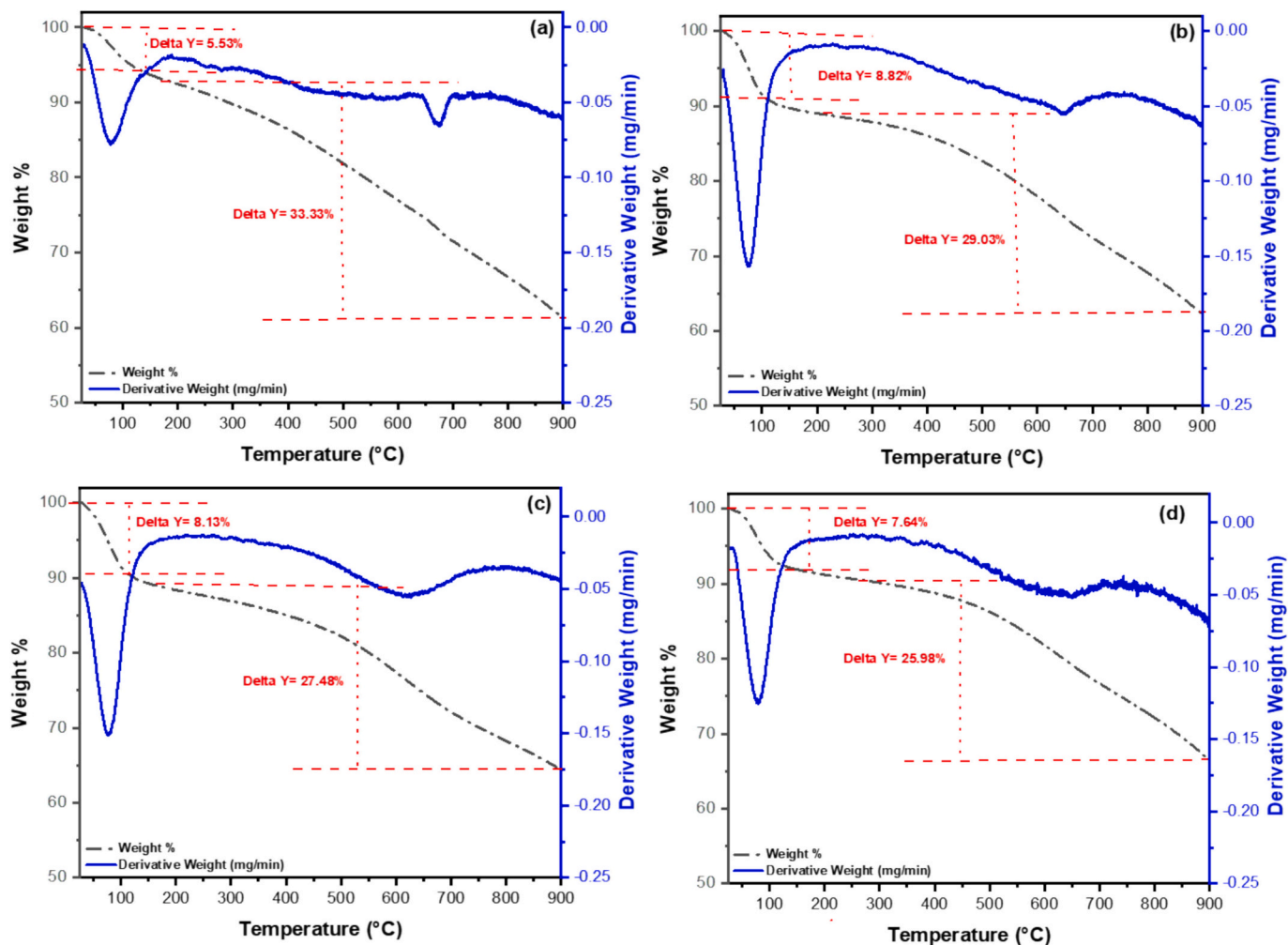


Fig. 5. TGA/DTA obtained data for the samples: (a) MP500, (b) 1 %TiO₂@MP500, (c) 2 %TiO₂@MP500, and (d) 3 %TiO₂@MP500.

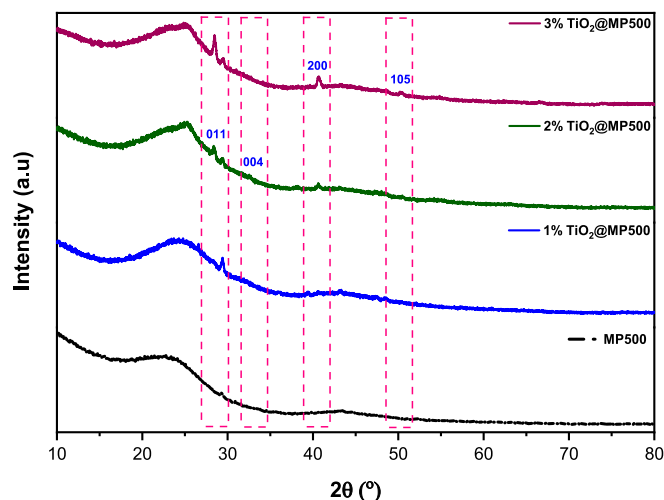


Fig. 6. XRD diffractogram of the as-prepared samples, including MP500, 1 %TiO₂@MP500, 2 %TiO₂@MP500, and 3 %TiO₂@MP500.

peak) in all samples, revealing structural changes with the graphitization process, and confirming the presence of MP500 biochar with TiO₂ in the impregnated sample. The D-peak reflects the defects with A_{1g} symmetry. In contrast, the G-peak is related to the E_{2g} phonon's first-

order scattering associated with sp²-hybridized carbon atoms [46,47]. The D-peak signals a disorder in the MP500 structure, and the G-peak signifies the graphitization. The I_D/I_G ratios for MP500, 1 %TiO₂@MP500, 2 %TiO₂@MP500, and 3 %TiO₂@MP500 are 0.74, 0.75, 0.78, and 0.78, correspondingly, demonstrating that 3 %TiO₂@MP500 exhibits a higher degree of defects due to the presence of TiO₂ nanoparticles on the surface which could affect the removal efficiency and the photocatalytic effectivity towards MO.

Fig. S1b highlights the Raman spectra (magnified) in the range between 100 and 1000 cm⁻¹. The obtained spectra showed the presence of TiO₂ vibrational peaks at 141 cm⁻¹, 392 cm⁻¹, 544 cm⁻¹, and 621 cm⁻¹, which are identified as the characteristic E_{1g}, B_{1g}, B_{1g}/A_{1g}, and E_{1g} vibrational modes of the anatase TiO₂, respectively [48]. The analysis indicates that the developed TiO₂ catalyst is pure without significant impurities. The observation of the E_{1g} peak in the Raman spectra of TiO₂@MP500 samples demonstrates the effective incorporation of the anatase form of the TiO₂ nanoparticles onto MP500, which is consistent with TGA analysis outcomes.

3.1.6. FTIR analysis

FTIR was applied to identify the chemical bonds in the synthesized MP500 before and after loading with TiO₂ and pinpoint the main functional groups within the prepared materials. Fig. 7 displays the FTIR spectra of MP500 and the nanocomposites. The spectrum of MP500 suggests the presence of carbonyl group (C=O) stretching in ketones and other compounds, which is apparent by the absorption band at 1568 cm⁻¹ [49]. Furthermore, the peak at 1377 cm⁻¹ is related to C – H

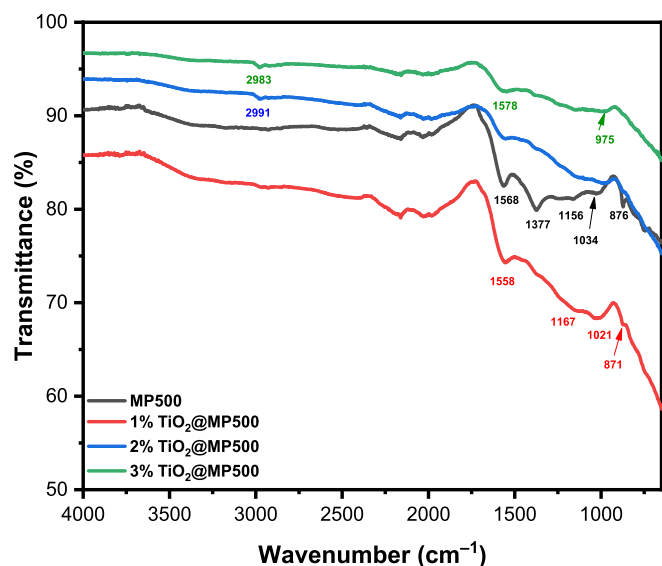


Fig. 7. FTIR spectra for MP500, 1 %TiO₂@MP500, 2 %TiO₂@MP500, and 3 %TiO₂@MP500.

bending vibrations, and peaks at 1156 and 1034 cm⁻¹ indicate C – O and C – O – C stretching, typical of cellulose-like structures [49]. On the other hand, the spectra of the TiO₂-impregnated sample show that TiO₂ exhibits an absorption band at 871 cm⁻¹, which corresponds to the anatase phase of TiO₂ and indicates the Ti – O – Ti stretching bond. Additionally, peaks between 1000 and 1300 cm⁻¹ are primarily associated with Ti–O–Ti vibrations, indicating the presence of O–Ti–O linkages [44]. The IR spectrum of the impregnated sample also shows the presence of MP500 bands with small shifts, such as the absorption at 1568 cm⁻¹ in MP500, which was shifted in 3 % TiO₂@MP500 to 1558 cm⁻¹. Other peaks at 1156 and 1034 cm⁻¹ in MP500 were also shifted to 1167 and 1021 cm⁻¹, which suggests the bonding between Ti (IV) ions and carboxyl groups, leading to a resonant structure for the carboxylate ion [50]. On the other hand, Fig. S2 shows a focus on the spectral range between 2500 cm⁻¹ and 3400 cm⁻¹. The obtained data reveal the presence of weak and slightly shifted peaks in both MP500 and 1 % TiO₂@MP500, appearing at 2970 cm⁻¹ and 2932 cm⁻¹ for MP500, and at 2970 cm⁻¹ and 2933 cm⁻¹ for 1 %TiO₂@MP500, corresponding to C–H stretching vibrations of aliphatic hydrocarbons [51,52]. The C–H stretching vibrations are also observed in the 2 %TiO₂@MP500 (at 2991 cm⁻¹ and 2965 cm⁻¹) and 3 %TiO₂@MP500 (at 2983 cm⁻¹ and 2969 cm⁻¹). The progression of these peaks from weak and broad peaks in MP500 and 1 %TiO₂@MP500 to more intense peaks in 2 % TiO₂@MP500 and 3 % TiO₂@MP500 highlights the role of TiO₂ loading in modifying the biochar surface. The obtained data confirm the successful formation of TiO₂ onto the surface of MP500.

3.2. Design analysis

The Box-Behnken (BB) design was employed in this study to tune the adsorbent/photocatalyst performance. As an experimental design, BB requires fewer runs compared to full-factorial designs, which in turn reduces the consumption of resources and hence the costs associated with materials, labor, equipment, and energy. This, in turn contributes to environmental sustainability and economic efficiency [35,36]. BB was exploited to investigate the effects of various independent variables on specific response variables. BB design ensures that each factor is tested at three equally spaced levels, high, medium, and low and coded as -1, 0, and +1. Table 1 showed the list of variables and their actual levels. The actual experimental responses, %R values, and the expected responses as well are listed in Table S2.

3.2.1. Quality tools

To analyze the BB design and decide on the significance of the studied variables, the Pareto chart was assessed, Fig. S3. Looking at the influence of the individual variables, all were significantly affecting the removal of MO with the adsorbent dose (B), pH (A), and the %TiO₂ – photocatalyst loaded on the substrate biochar surface (D), being the most statistically significant in the order mentioned.

By and large, increasing the adsorbent dose offers more spots for capturing the dye, MO. The influence of pH is also significant, inferring that the surface charge plays a role in the adsorption mechanism. The % TiO₂ loaded on the surface also considerably affects MO uptake. To that end, it cannot be decided whether these three variables possess a 'positive' or 'negative' influence on the uptake of MO. The squared and linear effects also highlight the significance of the tested variables. The squared effects of pH (AA) and the %TiO₂ loaded (DD) were the most influential squared variables. The linear effect, AD, for the interaction of pH (A) and the %TiO₂ loaded (D) was the most influential linear interaction. Nonetheless, a decision on the direction of this influence cannot be made from the Pareto chart.

The direction of the impact of each variable or variables' interactions, was evaluated using another quality tool, a normal plot of effects, Fig. S4. In this representation, variables on the left-hand side would exert a negative influence on the uptake of MO, in contrast to the variables on the right-hand side. The normal plot shows a positive effect of the adsorbent dose (B) on the removal of MO. In other words, an increase in the amount of adsorbent available to uptake MO is associated with higher %R. This could be ascribed not only to the active sites accessible for trapping the dye, but also to more substrate available for the immobilization of the photocatalyst–TiO₂, an issue which is contemplated as a better performance of the adsorbent/photocatalyst. The main effects plot – not shown, reveals that as the dose increases, the removal also increases till a certain dose, where a plateau is seen, and an almost constant performance is noticed afterward.

On the other hand, pH negatively affects the removal of MO, i.e., as the pH increases, the removal of MO decreases. The main effects plot shows a maximum at pH = 6 value, after which the removal starts to decline. In terms of adsorption, this finding needs to be addressed considering the pK_a of MO and the pH_{pzc} of the adsorbent, as well as the optimum conditions that will be determined from the final design analysis. Yet, considering the photocatalyst performance, this finding comes in agreement with the previous literature conclusions where extremely acidic or alkaline media deters the electrostatic repulsions sustaining the aggregation of the TiO₂ particles and diminishing the surface area available for adsorption and also the catalyst performance [53].

The %TiO₂ loaded on the surface also seems to have a positive effect on the degradation of MO to a certain level, after which the performance of the adsorbent starts to decline. In terms of adsorption, higher concentrations of the TiO₂ nanoparticles could clog the pores on the surface of the biochar, as apparent from the lower pore radii recorded for the 3 % TiO₂ composites compared to the 2 % and the 1 % counterparts, Table S3. Considering the photocatalysis, this also agrees with the literature, where at low concentrations of TiO₂, the concentration of the free radicals is expected to be low and would gradually increase while increasing the loading with TiO₂ [10,53]. At extremely high levels, the degradation efficacy starts to drop, most likely due to the aggregation of the nanoparticles impeding the light penetration into the active catalysis sites [54,55].

The initial concentration of MO also affects the removal process, yet with a lesser magnitude compared to the previous variables. The main effects plot shows that a steady increase in the removal is observed as the dye concentration increases to a certain level, after which the %R starts to decrease. This decrease could be interpreted in terms of adsorption, as saturation of the adsorbent's surface could occur at higher dye concentrations. In terms of photocatalysis, higher concentrations of the colored dye could absorb the light, masking the effect of TiO₂.

Other investigations of the linear variables' interaction and their impact on the uptake of MO were elaborated in both 2-dimensional and 3-dimensional formats. The former, collectively known as 'contour plot' is shown in Fig. 8. The right-hand-sided legend exhibits the %R as color codes, where the red and the maroon colors represent the highest MO removals. Looking at the significant interactions, for instance, the interaction of pH (A) and %TiO₂ (D), removal of 80–100 % of MO (red contour surface) is achieved using >2 % of TiO₂ (and <3 %) at pH range of ~5.8–6.2. This interaction and as could be concluded from the normal plot, has a positive influence on the removal of MO.

3.2.2. Modelling of adsorbent's performance

The product of design analysis using quality tools and ANOVA is a mathematical model that relates the removal of MO to the considered variables. Eq. (3) shows such a relationship in terms of coded effects. In this equation, λ denotes the transformation factor = 0.0664446.

$$\begin{aligned} \%R^{\lambda} = & 0.7764 + 0.05893 A + 0.002120 B + 0.001243C + 0.2690 D \\ & - 0.00162 E - 0.007522 A^2 - 0.000014 B^2 - 0.000011 C^2 \\ & - 0.10387 D^2 - 0.000038 E^2 - 0.000033 AB - 0.000046 AC \\ & + 0.01885 AD - 0.000367 AE - 0.000008 BC + 0.000367 BD \\ & + 0.000023 BE + 0.000169 CD + 0.000022 CE + 0.001282 DE \end{aligned} \quad (3)$$

Eq. (3) shows not only the direction of the influence of each variable but also the magnitude of this influence. Values of linearity indicators showed excellent linearity, with 0.9843 and 0.9706 for R² and adjusted R². Model power to expect any new trials was confirmed by the prediction indicator of 0.9395.

3.2.3. Optimum response findings

The desirability of a combination of the five tested variables

(simultaneously) was predicted by the *d*-function, but the figure is not shown. The relatively high value of *d* (0.99959) suggests that a combination of variables (pH ~ 6, AD ~97.78 mg, RT = 20 min, %TiO₂ of ~2.2 % and [MO] ~ 11.27 ppm) could achieve an adsorptive removal of ~94 % of MO. For the equilibrium and kinetics investigations, and since higher concentrations of MO will be used, 2–250 ppm, the 3 % TiO₂@MP500 will be utilized to ensure optimal performance over a wider range of [MO].

3.3. Equilibrium and kinetic studies

In this study, equilibrium isotherms were utilized to determine the quantity of MO adsorbed onto the 3 %TiO₂@MP500 surface and the nature of the MO-adsorbent interactions. The adsorption capacity of the 3 %TiO₂@MP500 under room temperature was examined through four equilibrium isotherms [56–59]. The Langmuir model commonly supports one of three primary assumptions:

1. Each adsorption site possesses the same energy to uptake MO.
2. A single MO molecule occupies a single site without any interactions between these molecules.
3. MO adsorption predominantly occurs on the surface of the adsorbent.

The Langmuir model can be demonstrated by Eq. (4) as follows:

$$q_e = \frac{q_m K_L C_e}{1 + K_L C_e} \quad (4)$$

Where q_m denotes the maximum adsorption capacity (in mg/g), and K_L stands for the Langmuir equilibrium constant (in L/mol). Additionally, the Langmuir model can be described with the Langmuir equilibrium constant as depicted in Eq. (5).

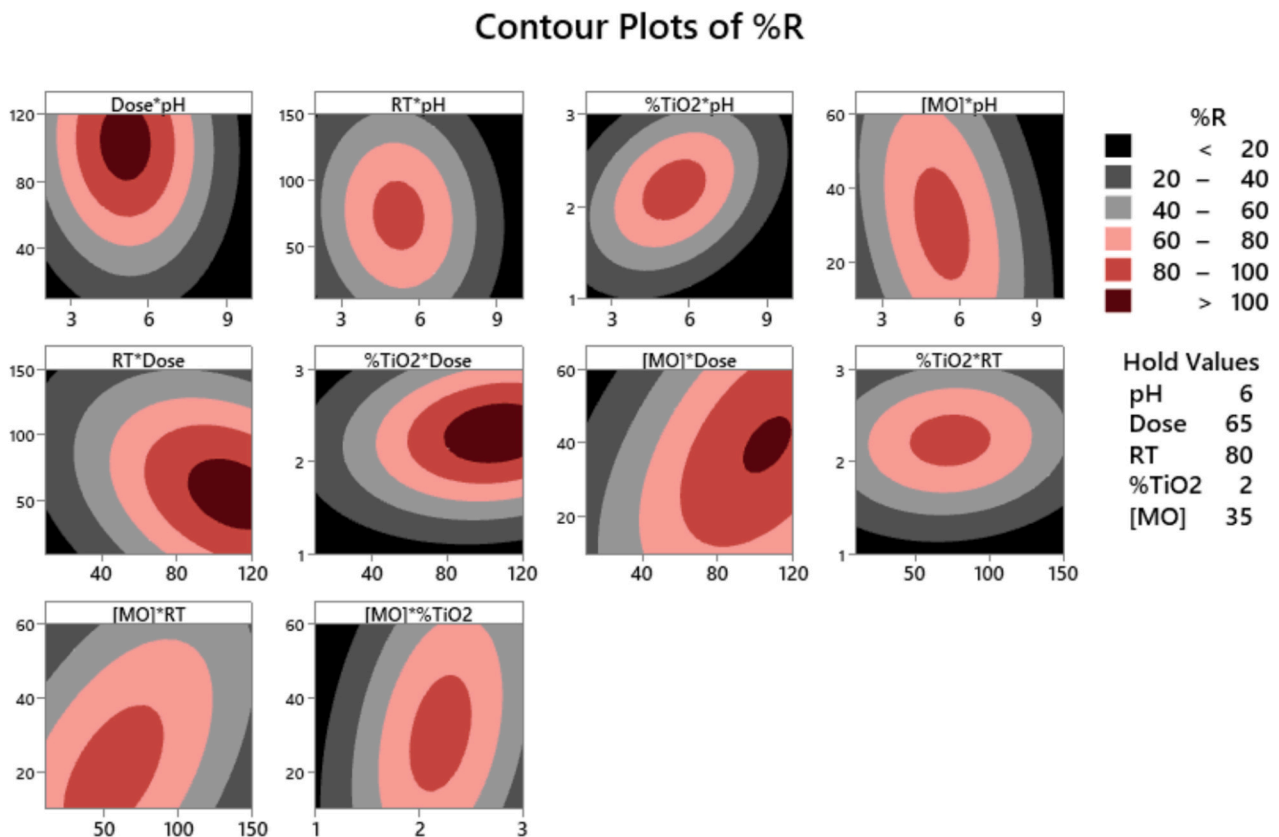


Fig. 8. Quality tool – Contour plot.

$$R_L = \frac{1}{1 + K_L C_0} \quad (5)$$

Thus, R_L and C_0 signify the separation factor and the initial [MO], respectively. R_L is utilized to evaluate the adsorption process's favorability. Specifically, an R_L value of 1 indicates an unfavorable sorption process, whereas a value between 0 and 1 suggests that the adsorption is favorable and occurs spontaneously. An R_L value of 0 implies that the reaction is irreversible. The computed R_L value for MO adsorption onto 3 %TiO₂@MP500 was <1, indicating a spontaneous and favorable adsorption process. Additionally, the adsorption of MO turned irreversible at high MO concentrations. The parameters listed in Table 2 reveal that the peak adsorption capacity for MO reached 104.2 mg/g.

Conversely, the Freundlich isotherm serves as an effective method for illustrating the energy distribution across a heterogeneous surface, as depicted in Eq. (6):

$$q_e = K_F C_e^{\frac{1}{n}} \quad (6)$$

Where C_e represents the equilibrium concentration of MO (mg/L) and q_e is the amount of MO adsorbed per unit of mass (mg/g), K_F (mole. g⁻¹) (L. mole⁻¹) denotes a constant, and $1/n$ is the Freundlich coefficient, which indicates the adsorption capacity and intensity variation, as well as the degree of deviation from linearity. According to the values reported in Table 2, the Freundlich coefficient $1/n$ equals 0.64, and n equals 1.56. The analysis demonstrates that MO adsorption onto 3 %TiO₂@MP500 aligns closely with the Freundlich isotherm model, evidenced by an R^2 value of 0.9956. This data affirms the exceptional adsorptive performance of 3 %TiO₂@MP500 towards MO. Consequently, the adsorption potential was calculated via Eq. (7) and found to be 3.86 kJ, indicating that 3 %TiO₂@MP500 will adsorb MO molecules with a potential energy of <3.86 kJ. Furthermore, this suggests that the MO adsorption process onto 3 %TiO₂@MP500 is favorable and irreversible.

$$A = n R T \quad (7)$$

The Temkin model is employed to characterize the interaction

Table 2

The resulting data from different models for MO adsorption onto 3 % TiO₂@MP500.

Model	Nonlinear equations	Parameters	Value
Langmuir	$q_e = \frac{q_m K_L C_e}{1 + K_L C_e}$	q_m (mg/g) K_L (L. mole ⁻¹) R^2	104.2 0.091 0.9884
Freundlich	$q_e = K_F C_e^{\frac{1}{n}}$	$1/n$ K_F (mole/g) (L/mol) ^{1/n} R^2	0.64 10.95 0.9956
Temkin	$q_e = \frac{RT}{b_T} \ln(A_T C_e)$	b_T (J/mol) A_T (L/mol) R^2	287.9 11.77 0.8102
D-R	$q_e = q_s \cdot \exp.(-\beta \cdot \epsilon^2)$	β	1.18×10^{-8}
	$\epsilon = RT \left(1 + \frac{1}{C_e}\right)$	E (kJ/mol)	6.51
	$E = 1/\sqrt{2\beta}$	q_m (mg/g) R^2	51.93 0.9133
Pseudo-first order (PFO)	$\frac{dq_t}{dt} = k_1(q_e - q_t)$	K_1 (min ⁻¹) q_e (mg/g) R^2	0.017 32.93 0.8765
Pseudo-second order (PSO)	$\frac{dq_t}{dt} = k_2(q_e - q_t)^2$	K_2 (g.mg ⁻¹ . min ⁻¹) q_e (mg/g) R^2	0.018 35.29 0.9731
Elovich model	$q_t = \frac{1}{\beta} \times \ln(1 + \alpha \beta t)$	α β R^2	367.8 0.244 0.8647
Weber-Morris model	$q_t = K_t t^{0.5} + C$	K_t C R^2	1.62 21.52 0.6282

between the MO and 3 %TiO₂@MP500 adsorbent, as can be detailed by the subsequent Eq. (8):

$$q_e = \frac{RT}{b_T} \ln(A_T C_e) \quad (8)$$

Where R denotes the universal gas constant, A_T is the equilibrium binding constant, b_T measures the energy of adsorption, and T represents the temperature in Kelvin (K). The sorption energy for MO is calculated to be 287.9 J/mol (Fig. 9a and Table 2). These findings indicate that the adsorption of MO onto the surface of the 3 %TiO₂@MP500 adsorbent is favorable.

The Dubinin–Radushkevich (D-R) model was used to explore the mechanism of the MO dye adsorption onto the 3 % TiO₂@MP500 adsorbent, which is articulated through Eq. (9):

$$q_e = q_s \cdot \exp.(-\beta \cdot \epsilon^2) \quad (9)$$

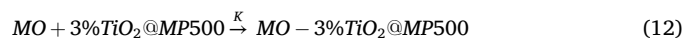
Within this formula, q_s signifies the highest MO adsorption capacity, while β serves as the activity coefficient, functioning to evaluate the energy of adsorption, E , in kJ/mol. Furthermore, ϵ represents the Polanyi potential. Eqs. (10) and (11) were used to illustrate the potential energy of adsorption alongside the Polanyi potential as follows:

$$\epsilon = RT \left(1 + \frac{1}{C_e}\right) \quad (10)$$

$$E = 1/\sqrt{2\beta} \quad (11)$$

Hence, according to the information presented in Table 2, the findings related to MO dye show a sorption energy of 6.51 kJ/mol, suggesting that the MO adsorption mechanism on 3 %TiO₂@MP500 is predominantly physisorption, characterized by a sorption energy of <8 kJ/mol. Such results imply that the efficiency of MO adsorption onto the 3 %TiO₂@MP500 relies on the adsorbent's surface area.

The investigation into MO adsorption onto 3 %TiO₂@MP500 nanocomposite encompassed analysis through four kinetic models [60–62]. Fig. 9b and Table 2 present the correlation between q_t (mg/g) and time (t , min) for MO adsorption onto 3 %TiO₂@MP500, alongside the derived metrics for each model. The findings highlight that the pseudo-second order model exhibits the most substantial correlation coefficient ($R^2 = 0.9731$). This data suggests that the MO adsorption on 3 % TiO₂@MP500 is influenced by the concentrations of both MO and the 3 %TiO₂@MP500 adsorbent, which is mathematically depicted in Eq. (12):



Conversely, the R^2 values for other models, such as Elovich and Weber Morris, were markedly lower in comparison to those of PSO and PFO, registering at 0.8647 for Elovich and 0.6282 for Weber Morris. These significantly lower correlations indicate that these models are inadequate for characterizing MO adsorption onto 3 % TiO₂@MP500.

3.4. Photocatalytic activity of TiO₂@MP500 nanocomposites

In this study, photocatalysis was employed to enhance the decolorization rate of MO. The combined analysis of adsorption kinetics and optimization of the process design revealed that nearly complete decolorization of MO was possible after maintaining contact with 3 % TiO₂@MP500 for a duration of 120 min. Further examination of the kinetics of photocatalysis indicated that under UV light exposure, the MO-3 %TiO₂@MP500 system, the decolorization of MO was nearly complete within a much shorter timeframe of 30 min.

Further, in alignment with BB design findings that identified 3 % TiO₂@MP500 as the most efficient adsorbent, Fig. 10 illustrates that the highest MO decolorization efficiency (%DE) was achieved with 3 % TiO₂@MP500. After 10 min under UV light, >90 % of MO was degraded,

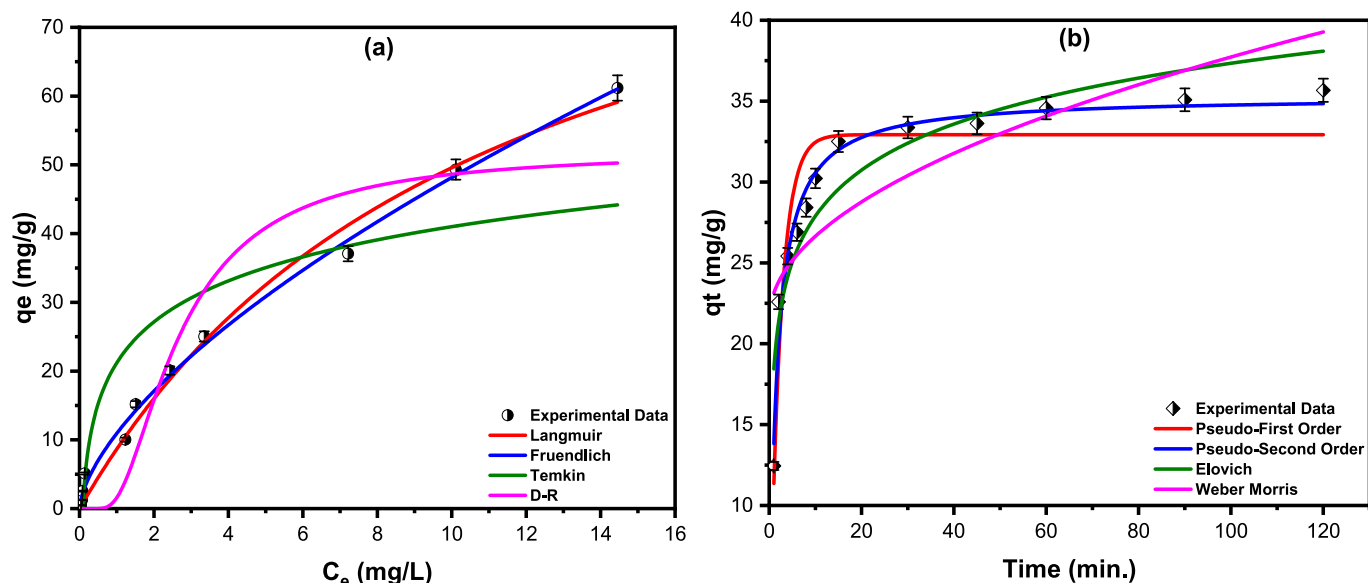


Fig. 9. (a) Equilibrium and (b) kinetic studies for the adsorption of MO onto 3 %TiO₂@MP500.

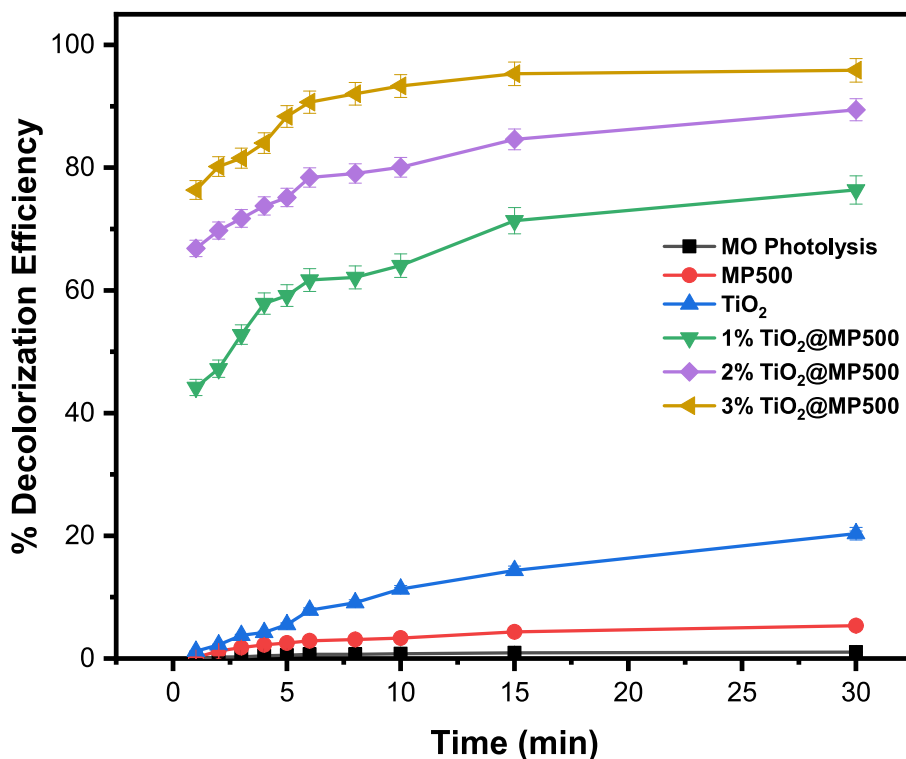


Fig. 10. Direct photolysis of MO, the decolorization efficiency of pristine biochar (MP500), pristine TiO₂, and the three nanocomposites (with 1, 2, and 3 % TiO₂) under UV light.

and a maximum decolorization was recorded at 30 min. The decolorization efficiency approached complete (98.87 %) compared to 89.32 % and 76.54 % for the 2 % and 1 % variants, respectively. Fig. 10 also showed that the photolysis of MO (standalone with no adsorbent) was almost negligible under UV light, demonstrating the stability of MO in the presence of UV light [63–65]. On the other hand, the MO-MP500, and the pristine TiO₂ systems under UV light exposure showed a low %DE of <5 %, and 20.38 %, after 30 min, respectively, which could have resulted from the adsorption process in the case of the MP500 sample, confirming that the photocatalytic effect is due to the presence of TiO₂

nanoparticles on the surface of the biochar. In the case of the pure TiO₂, a single mechanism – photocatalysis – is taking place with no adsorptive support [66,67].

Fig. 11a shows the kinetics of the photocatalysis activity of 3 % TiO₂@MP500 towards MO. The relationship between $\ln(C_0/C_t)$ and time (t , min) conformed to a first-order kinetics model, as specified in Eq. (13).

$$\ln(C_0/C_t) = k_1 t \quad (13)$$

C_0 and C_t denote the initial MO concentration and MO concentration

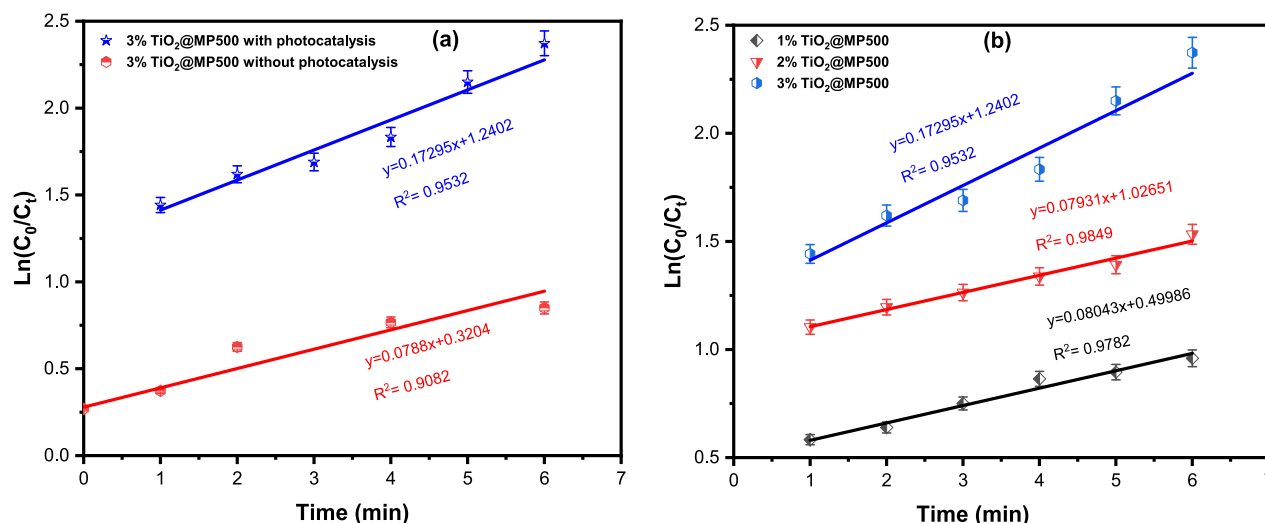


Fig. 11. (a) Photocatalytic kinetics of MO using 3 % TiO_2 @MP500 versus kinetics of the same sample with adsorption only for contact time of 6 min, and (b) Photocatalytic decolorization kinetics of MO using TiO_2 @MP500 photocatalyst.

after a specific duration under photocatalytic conditions or the equilibrium concentration after adsorption without photocatalysis, respectively, measured in ppm. The rate constant k_1 (min^{-1}), derived from the linear regression slope, and time (t , min) are critical parameters. A notable rise in the k_1 value from the linear graphs was observed, with a decolorization rate constant of 0.1729 min^{-1} , about 2.2 times faster than decolorization through adsorption alone. This comparative experiment highlights a synergistic impact between MP500 and TiO_2 nanoparticles, with the presence of TiO_2 enhancing the decolorization rate of MO, likely due to its anatase crystal structure.

The study also investigated how increasing the TiO_2 concentration (%) on the MP500 surface affects the kinetics of photocatalysis, as shown in Fig. 11b. The analysis of the rate constants across different slopes revealed that 3 % TiO_2 @MP500 outperformed its 2 % and 1 % counterparts. This indicates that a higher TiO_2 concentration on the MP500 surface, up to 3 %, enhances the presence of the anatase form of TiO_2 , as also evident in SEM images showing TiO_2 layers covering the surface at 3 % TiO_2 @MP500. The resulting data shown in Fig. 11b also showed high values of R^2 , suggesting that this model can accurately describe the kinetics of the MO decomposition. Lower photocatalytic activity of the 1 % and 2 % TiO_2 , compared to the 3 % TiO_2 , could be a result of the MP500 biochar's shielding effect, which potentially obstructs light from reaching the photocatalyst's surface, suggesting 3 % TiO_2 as the optimal concentration for photocatalyst synthesis. These outcomes underline the significance of determining the optimal TiO_2 concentration as part of the preceding BB design optimization.

3.5. Proposed adsorption and photocatalysis mechanisms

The mechanism of MO adsorption onto 3 % TiO_2 @MP500 involves multiple pathways, including hydrogen bonding, electrostatic, and π - π interactions, hydrophobic effects, and ion exchange [68]. The π - π interactions arise from the interaction between the aromatic rings of MO and the aromatic structure of the biochar (carbonaceous backbone). Electrostatic interactions are facilitated by the bonding of MO with surface functional groups on the 3 % TiO_2 @MP500, such as $\text{C}=\text{O}$, $\text{C}-\text{O}$, $\text{C}-\text{O}-\text{C}$, $\text{Ti}-\text{O}-\text{Ti}$, and $\text{O}-\text{Ti}-\text{O}$, as confirmed by the FTIR analysis. The adsorption process is further enhanced by the high surface area of the 3 % TiO_2 @MP500 nanocomposite ($184.61 \text{ m}^2/\text{g}$). The high surface area of the 3 % TiO_2 @MP500 compared to the pristine biochar and to the 1 % and 2 % counterparts implies availability of more active sites for capturing MO. The point of zero charge (pH_{PZC}) of the adsorbent plays a significant role in determining the adsorption mechanism. To evaluate

the surface charge of the 3 % TiO_2 @MP500 nanocomposite, a graph plotting the initial pH against the final pH was constructed (Fig. S5). The pH_{PZC} of 3 % TiO_2 @MP500 was found to be 5.82, while the optimum pH as determined employing BB design, was 6.0. At this pH, the nanocomposite's surface is nearly neutral, indicating that electrostatic interactions are unlikely to be the dominant mechanism for MO adsorption. Instead, the large surface area of the nanocomposite facilitates physisorption, as confirmed by equilibrium findings.

For the photocatalytic process, TiO_2 nanoparticles on the surface of the biochar act as a semiconductor photocatalyst. Upon UV irradiation, electrons in the valence band (VB) are excited to the conduction band (CB), leaving holes (h^+) in the VB. The energy required for the electron excitation corresponds to the TiO_2 band gap. The produced photo-generated electron-hole pairs resulted in a redox reaction at the TiO_2 surface [69]. The electrons in the CB reduce the dissolved oxygen molecules to form superoxide radicals ($\text{O}_2^{\cdot -}$), producing reactive species like hydroxyl radicals (OH^{\cdot}) [70]. Similarly, the holes in the VB oxidize water molecules or hydroxide ions to generate additional hydroxyl radicals. These reactive oxygen species are highly oxidative and break down the MO molecules into CO_2 and H_2O [71]. Combination of biochar as adsorbent with TiO_2 as a photocatalyst brings advantages of both. In this combination, the biochar acts as a support material for TiO_2 , allowing the concentration of MO on the surface of the biochar and hence facilitates the dye exposure to the photocatalyst effect. Furthermore, having the biochar backbone diminish the aggregation of the photocatalyst nanoparticles [22,23]. The dual mechanism of adsorption and photocatalysis makes 3 % TiO_2 @MP500 a highly effective nanocomposite for MO removal.

3.6. Regeneration and reusability

The feasibility of using any adsorbent economically relies mainly on its ability to be regenerated, a factor primarily estimated through adsorbent regeneration studies. A desorption study was conducted with five different eluents, and the adsorbent 3 % TiO_2 @MP500 was regenerated through six rounds of adsorption-desorption cycles. The study evaluated the efficacy of desorbing MO from 3 % TiO_2 @MP500 using five eluents: 0.1 M of HCl , Na_2CO_3 , and H_2SO_4 , 10 % ethanol ($\text{C}_2\text{H}_5\text{OH}$), and DI water. Fig. 12a illustrates the effectiveness of the investigated eluents in the MO desorption process, indicating that 0.1 M HCl was the most effective eluent, achieving a 97.88 % desorption efficiency, whereas 0.1 M H_2SO_4 achieved 87.66 % efficacy. Consequently, 0.1 M HCl was selected as the prime eluent for desorbing MO from MO-loaded

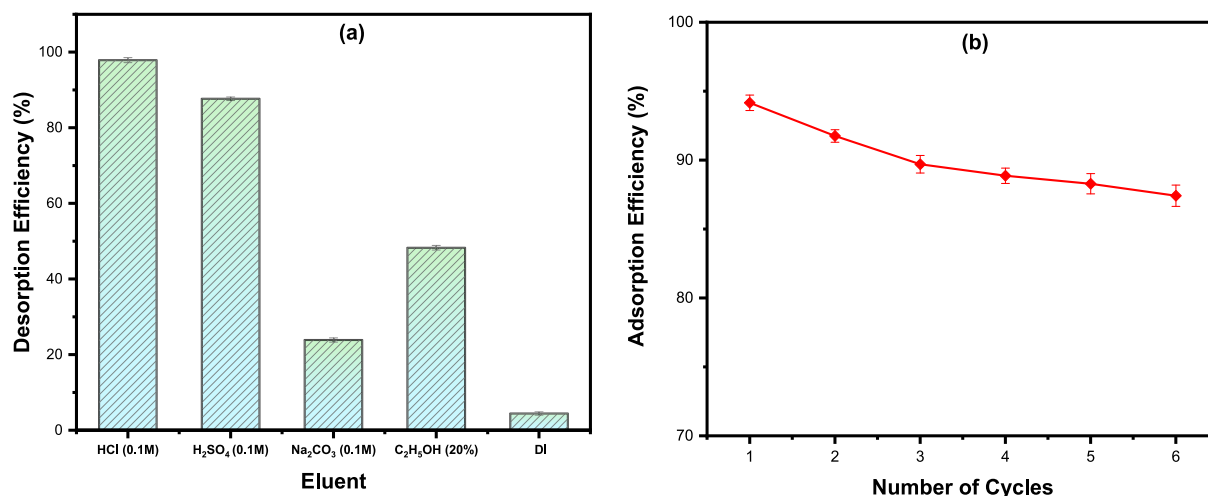


Fig. 12. (a) Elution of MO from loaded 3 %TiO₂@MP500 using various eluents, and (b) The regeneration and 3 %TiO₂@MP500 adsorbent for removing MO.

3 %TiO₂@MP500.

The highest desorption efficiency was realized using 0.1 M HCl as an eluent solution because, at a pH value of ~1, which is lower than the pKa of MO (~3.4), the sulfonate and azo functional groups of MO are protonated, reducing their negative charge and weakening the electrostatic interactions with the functional groups of 3 %TiO₂@MP500, leading to an improved desorption efficiency [72–74]. On the other hand, Na₂CO₃ exhibits low desorption efficiency where the pH of Na₂CO₃ is higher than the pKa of the MO, resulting in deprotonation of MO's sulfonate group and enhancing the electrostatic binding to the adsorbent surface and decreasing the desorption efficiency. Similarly, DI water shows a very low desorption efficiency because of its neutral pH (~7), which does not affect the electrostatic interactions.

Furthermore, cyclic adsorption-desorption experiments were performed to assess the regenerative capabilities of the 3 %TiO₂@MP500 adsorbent, Fig. 12b. The obtained results highlighted a slight defect in the MO removal, from 95.42 % in the first cycle to 90.91 % in the sixth cycle. These outcomes highlight the adsorbent's stability and efficient regenerative potential, maintaining over 85 % removal efficiency across more than six cycles.

3.7. Comparison of the removal efficiency of MO with literature

A comparison between the current approach for remediating MO-polluted wastewater and the literature efforts is revealed in Table 3. Data exhibited in the table shows that the developed adsorbent is superior to most of the reported approaches in terms of its adsorption capacity. Moreover, compared to the commercial activated carbon, the current adsorbent shows almost the same performance. In terms of photocatalytic behavior, the developed composite shows an excellent performance in terms of degradation efficiency, the time needed for degradation, and the degradation rate constant.

3.8. Economic analysis

The main target of preparing the 3 %TiO₂@MP500 derived from the waste mandarin peels and TiO₂ highlights its potential for use on a large scale at a reasonable cost. Preparation of this material involves the synthesis of an eco-biochar, MP500, via pyrolysis of the waste peels at 500 °C, followed by loading of TiO₂ using the hydrothermal synthesis. The current investigation, therefore, highlights the value of reusing waste biomasses and production of advanced materials for environmental protection, water purification, and catalytic processes under the umbrella of circular economy and sustainability [40].

The estimated energy consumption for manufacturing 10 kg of

Table 3

A comparison between the current approach and the reported methods for the removal of MO via adsorption, photocatalysis, and integrated adsorption-photocatalysis.

Adsorbent Biochar	Adsorption Capacity	Reference
Mandarin peels	104.2 mg/g	Current study
Sheep manure	42.513–45.563 mg/g	[75]
Pistachio nutshells	142.38 mg/g	[10]
Sawdust biochar	136.67 mg/g	[76]
Orange peels	15.8 mg/g	[77]
Banana peels	17.2 mg/g	[77]
Waste of <i>Prosopis juliflora</i>	8.08 mg/g	[78]
Commercial activated carbon	129.3 mg/g	[79]

TiO ₂ – Photocatalyst	Performance Indicators	Reference
TiO ₂ @ biochar of mandarin peels	Degradation rate constant: $17.29 \times 10^{-2} \text{ min}^{-1}$ %DE: 98.87 %, < 30 min	Current study
TiO ₂ @ biochar of pistachio nut shells	Degradation rate constant: $12.74 \times 10^{-2} \text{ min}^{-1}$ %DE: 99.47 %, 30 min (using UV lamp with power of 4 W, and at a wavelength of 245 nm)	[10]
Commercial, thermally treated TiO ₂ , anatase	Degradation rate constant of 2.6683 h^{-1} (using solar intensity of 815 W)	[80]
TiO ₂ @ biochar of shells of walnut	Degradation rate constant: $2.26 \times 10^{-2} \text{ min}^{-1}$ %DE: 96.88 %, 150 min (using lamp light with power of 500 W, and at a wavelength 360 nm)	[81]
TiO ₂ @ biochar of corn straws	Degradation rate constant: $7.69 \times 10^{-3} \text{ min}^{-1}$ %DE: 97.98 %, 270 min (using a 300 W xenon lamp which produces sunlight in the ultraviolet region: 6.6 W; and the visible region: 17.6 W)	[66]

MP500 biochar is 174.6 (kW h), with an electricity tariff of 0.024 \$/kW h (as of 2024, Qatar), which includes energy consumed by the oven and the furnace. The total cost per kg of MP500 was found to be 0.419\$. The reagents used in preparing 11 g of 3 %TiO₂@MP500 were oleylamine, n-propanol, TiCl₄, and ammonia solutions, with a cost of 0.168 \$, 1.015 \$, 5.30 \$, and 0.207 \$, respectively. The total cost of one gram of 3 %TiO₂@MP500 was 0.61 \$. The results show low production expenses per kilogram of MP500 biochar and TiO₂@MP500 nanocomposites. Compared to nanocomposites in the market and considering that this value is estimated on the lab scale, costs will decrease when prepared on

a large scale, considering that the biochar is prepared from waste material, which is almost costless. This substantial cost reduction provides an advantage within the market, potentially making nanocomposites more accessible and widely used across industries. Ensuring this production process can be scaled up effectively is essential for sustainability.

Utilizing waste mandarin peels, a leftover from the fruit juice industry, as a biochar precursor not only minimizes waste accumulation but also cuts down on raw material expenses. However, expanding production requires logistics planning, such as ensuring a supply of mandarin peel waste and setting up efficient transportation and processing systems for managing this waste. Furthermore, the environmental advantages of this approach add to its significance. Transforming waste into a product like 3 %TiO₂@MP500 aligns with circular economy and sustainability principles.

To conclude, manufacturing 3 %TiO₂@MP500 presents an argument for broad-scale implementation due to its cost-efficient production process, sustainability benefits, and promising market prospects. To make it economically sustainable, we need to tackle issues like expanding the business, reaching customers, and ensuring a flow of resources.

4. Conclusion

A highly efficient material with a dual role, adsorbent and photocatalyst, was developed using mandarin waste peels. The TiO₂@MP500 acted as an effective adsorbent and photocatalyst for the removal of MO from wastewater. The Box-Behnken design demonstrated that TiO₂@MP500 achieved an adsorption efficiency of 93.96 % under optimal conditions, which included a pH of 6, adsorbent dose of 97.78 mg, reaction time of 20 min, 2.2 % TiO₂, and an initial MO concentration of 11.27 ppm. The unique structure of 3 %TiO₂@MP500, along with its large surface area, enhances the adsorption of MO, resulting in increased photocatalytic activity. Analysis of the adsorption equilibrium models revealed that the 3 %TiO₂@MP500 nanocomposites exhibited a predominantly physical adsorption mechanism. The adsorption of MO followed the Freundlich model, as evidenced by an R²-value of 0.9956. The photocatalytic performance indicated that 3 %TiO₂ exhibits higher photocatalytic activity compared to 1 % and 2 % TiO₂, with a rate constant of $17.29 \times 10^{-2} \text{ min}^{-1}$. The precise preparation and synthesis process of the nanocomposite, along with its effective adsorption and photocatalytic degradation capabilities, make it an attractive option for the removal and degradation of MO. Scalability and application to real wastewater are the main limitations of the current investigation. Further investigations in real-life scenarios where more than one pollutant could exist are needed. These limitations will be addressed in future research.

CRedit authorship contribution statement

Marwa Ezzine: Writing – review & editing, Writing – original draft, Visualization, Validation, Methodology, Investigation, Formal analysis, Data curation. **Ahmed S. El-Shafie:** Writing – review & editing, Writing – original draft, Visualization, Validation, Supervision, Software, Resources, Project administration, Methodology, Investigation, Formal analysis, Data curation, Conceptualization. **Khaled M. Youssef:** Writing – review & editing, Writing – original draft, Validation, Supervision, Resources, Formal analysis, Data curation, Conceptualization. **Marwa El-Azazy:** Writing – review & editing, Writing – original draft, Visualization, Validation, Supervision, Software, Resources, Project administration, Methodology, Investigation, Formal analysis, Data curation, Conceptualization.

Declaration of competing interest

The authors declare that they have no known competing financial interests or personal relationships that could have appeared to influence

the work reported in this paper.

Acknowledgments

The project members would like to extend their special thanks to the Central Lab Unit (CLU) at Qatar University. Open Access funding provided by the Qatar National Library.

Appendix A. Supplementary data

Supplementary data to this article can be found online at <https://doi.org/10.1016/j.ijbiomac.2025.141753>.

Data availability

All data used to support the findings of this study are included within the article.

References

- [1] Y. Song, L. Wang, X. Qiang, W. Gu, Z. Ma, G. Wang, An overview of biological mechanisms and strategies for treating wastewater from printing and dyeing processes, *J. Water Process Eng.* 55 (2023) 104242.
- [2] J.O. Ighalo, C.A. Adeyanju, S. Ogunniyi, A.G. Adeniyi, S.A. Abdulkareem, An empirical review of the recent advances in treatment of natural fibers for reinforced plastic composites, *Compos. Interf.* 28 (9) (2021) 925–960.
- [3] H. Solayman, M.A. Hossen, A. Abd Aziz, N.Y. Yahya, L.K. Hon, S.L. Ching, M. U. Monir, K.-D. Zoh, Performance evaluation of dye wastewater treatment technologies: a review, *J. Environ. Chem. Eng.* 11 (3) (2023) 109610.
- [4] N. Bahrudin, M. Nawi, Z. Zainal, Insight into the synergistic photocatalytic-adsorptive removal of methyl orange dye using TiO₂/chitosan based photocatalyst, *Int. J. Biol. Macromol.* 165 (2020) 2462–2474.
- [5] M.F. Hanafi, N. Sapawe, A review on the water problem associate with organic pollutants derived from phenol, methyl orange, and remazol brilliant blue dyes, *Materials Today Proc.* 31 (2020) A141–A150.
- [6] S.S. Emmanuel, A.A. Adesibikan, E.A. Opatola, C.O. Olawoyin, A pragmatic review on photocatalytic degradation of methyl orange dye pollutant using greenly bio-functionalized nano-metallic materials: a focus on aquatic body, *Appl. Organomet. Chem.* 37 (7) (2023) e7108.
- [7] U. Ewuzie, O.D. Saliu, K. Dulta, S. Ogunniyi, A.O. Bajeh, K.O. Iwuozor, J.O. Ighalo, A review on treatment technologies for printing and dyeing wastewater (PDW), *J. Water Process Eng.* 50 (2022) 103273.
- [8] B.S. Rath, P.S. Kumar, Sustainable approach on the biodegradation of azo dyes: a short review, *Curr. Opin. Green Sustain. Chem.* 33 (2022) 100578.
- [9] M. Berradi, R. Hsissou, M. Khudhair, M. Assouag, O. Cherkaoui, A. El Bachiri, A. El Harfi, Textile finishing dyes and their impact on aquatic environments, *Heliyon* 5 (11) (2019).
- [10] A.S. El-Shafie, M. Abouseada, M. El-Azazy, TiO₂-functionalized biochar from pistachio nutshells: adsorptive removal and photocatalytic decolorization of methyl orange, *Appl. Water Sci.* 13 (12) (2023) 227.
- [11] I. Obiora-Okafor, O. Onukwuli, Optimization of coagulation-flocculation process for colour removal from azo dye using natural polymers: response surface methodological approach, *Niger. J. Technol.* 36 (2) (2017) 482–495.
- [12] N. Neethu, T. Choudhury, Treatment of methylene blue and methyl orange dyes in wastewater by grafted titania pillared clay membranes, *Recent Pat. Nanotechnol.* 12 (3) (2018) 200–207.
- [13] L. Ayed, E. Khelifi, H.B. Jannet, H. Miladi, A. Cheref, S. Achour, A. Bakhrouf, Response surface methodology for decolorization of azo dye methyl Orange by bacterial consortium: produced enzymes and metabolites characterization, *Chem. Eng. J.* 165 (1) (2010) 200–208.
- [14] A.H. Birniwa, U. Ali, B.M. Jahun, B.N.S. Al-dhawi, A.H. Jagaba, Cobalt oxide doped polyaniline composites for methyl orange adsorption: optimization through response surface methodology, *Case Stud. Chem. Environ. Eng.* 9 (2024) 100553.
- [15] N.N. Abd Malek, A.H. Jawad, A.S. Abdulhameed, K. Ismail, B. Hameed, New magnetic Schiff's base-chitosan-glyoxal/fly ash/Fe₃O₄ biocomposite for the removal of anionic azo dye: an optimized process, *Int. J. Biol. Macromol.* 146 (2020) 530–539.
- [16] S.A.B. Gilani, F. Naseeb, A. Kiran, M.U. Ihsan, J. Iqbal, H.M.A. Javed, H.N. Bhatti, A.M. Karami, S. Hussain, M. ShabirMahar, pH dependent synthesis of ceria nanoparticles for efficient sunlight-driven photocatalysis of methyl orange containing wastewater, *Opt. Mater.* 148 (2024) 114871.
- [17] A. Najafidoust, M. Haghighi, E.A. Asl, H. Bananifard, Sono-precipitation dispersion of CuO-doped ZnO nanostructures over SiO₂-aerogel for photo-removal of methylene blue, Congo red and methyl orange from wastewater, *J. Ind. Eng. Chem.* 131 (2024) 346–359.
- [18] Z. Deng, B. Zhao, S. Li, Z. Li, S. Zhang, K. Zhang, Z. Zhu, An efficient CuZr-based metallic glasses electrode material for electrocatalytic degradation of azo dyes, *J. Environ. Sci.* 136 (2024) 537–546.

- [19] X. Li, J. Chen, Y. Wang, Z. Cheng, X. Chen, X. Gao, M. Guo, Porous spherical Cu₂O supported by wood-based biochar skeleton for the adsorption-photocatalytic degradation of methyl orange, *Appl. Surf. Sci.* 611 (2023) 155744.
- [20] T. Kou, Y. Wang, C. Zhang, J. Sun, Z. Zhang, Adsorption behavior of methyl orange onto nanoporous core-shell Cu@Cu₂O nanocomposite, *Chem. Eng. J.* 223 (2013) 76–83.
- [21] D.B. Miklos, C. Remy, M. Jekel, K.G. Linden, J.E. Drewes, U. Hübner, Evaluation of advanced oxidation processes for water and wastewater treatment—a critical review, *Water Res.* 139 (2018) 118–131.
- [22] J. You, C. Liu, X. Feng, B. Lu, L. Xia, X. Zhuang, In situ synthesis of ZnS nanoparticles onto cellulose/chitosan sponge for adsorption–photocatalytic removal of Congo red, *Carbohydr. Polym.* 288 (2022) 119332.
- [23] D. Keane, S. Basha, K. Nolan, A. Morrissey, M. Oelgemöller, J.M. Tobin, Photodegradation of famotidine by integrated photocatalytic adsorbent (IPCA) and kinetic study, *Catal. Lett.* 141 (2011) 300–308.
- [24] N. Yahya, F. Aziz, N. Jamaludin, M. Mutalib, A. Ismail, W. Salleh, J. Jaafar, N. Yusof, N. Ludin, A review of integrated photocatalyst adsorbents for wastewater treatment, *J. Environ. Chem. Eng.* 6 (6) (2018) 7411–7425.
- [25] J.-h. Sun, Y.-k. Wang, R.-x. Sun, S.-y. Dong, Photodegradation of azo dye Congo red from aqueous solution by the WO₃-TiO₂/activated carbon (AC) photocatalyst under the UV irradiation, *Mater. Chem. Phys.* 115(1) (2009) 303–308.
- [26] H. Belayachi, B. Bestani, N. Benderdouche, M. Belhakem, The use of TiO₂ immobilized into grape marc-based activated carbon for RB-5 azo dye photocatalytic degradation, *Arab. J. Chem.* 12 (8) (2019) 3018–3027.
- [27] M.-J. Suh, Y. Shen, C.K. Chan, J.-H. Kim, Titanium Dioxide-Layered Double Hydroxide Composite Material for Adsorption–Photocatalysis of Water Pollutants, *Langmuir* 35 (26) (2019) 8699–8708.
- [28] T. Sultana, S.C. Dey, M.A.I. Molla, M.R. Hossain, M.M. Rahman, M.S. Quddus, M. Moniruzzaman, S.M. Shamsuddin, M. Sarker, Facile synthesis of TiO₂/chitosan nanohybrid for adsorption-assisted rapid photodegradation of an azo dye in water, *React. Kinet. Mech. Catal.* 133 (2) (2021) 1121–1139.
- [29] E. Mekatel, N. Dahdouh, A. Samira, D. Nibou, M. Trari, Removal of Maxilon red dye by adsorption and photocatalysis: optimum conditions, equilibrium, and kinetic studies, *Iran. J. Chem. Chem. Eng.* 40 (1) (2021) 93–110.
- [30] A.S. El-Shafie, R. Mahmoud, I. Ahsan, H. Hamdi, M.F. Shibli, M. El-Azazy, Removal of antibiotics from aqueous solutions: insights of competitive adsorption onto Ni-impregnated biochar of spent coffee grounds, *Appl. Water Sci.* 14 (9) (2024) 209.
- [31] A.S. El-Shafie, F.G. Barah, M. Abouseada, M. El-Azazy, Performance of pristine versus magnetized orange peels biochar adapted to adsorptive removal of daunorubicin: eco-structuring, kinetics and equilibrium studies, *Nanomaterials* 13 (9) (2023) 1444.
- [32] T. Unugul, F.U. Nigiz, Preparation and characterization an active carbon adsorbent from waste mandarin peel and determination of adsorption behavior on removal of synthetic dye solutions, *Water Air Soil Pollut.* 231 (11) (2020) 538.
- [33] N.C. Özdemir, Z. Bilici, M. Saleh, N. Dizge, Adsorption of phosphate ions and RBBR dye from aqueous solution using thermally activated mandarin peel waste, *Water Pract. Technol.* 19 (1) (2024) 170–180.
- [34] A.H. Jawad, S.N. Jumadi, L.D. Wilson, Z.A. AlOthman, Optimization of methylene blue removal by H₃PO₄ thermochemically treated mixed pineapple peel and algae adsorbent and insight on the adsorption mechanism, *Biomass Convers. Biorefinery* (2024) 1–15.
- [35] A.S. El-Shafie, M. El-Azazy, Crosslinked chitosan–montmorillonite composite and its magnetized counterpart for the removal of basic fuchsin from wastewater: parametric optimization using box-Behnken design, *Int. J. Biol. Macromol.* 263 (2024) 130224.
- [36] A.-T. Mohammad, A.S. Abdulhameed, A.H. Jawad, Box-Behnken design to optimize the synthesis of new crosslinked chitosan-glyoxal/TiO₂ nanocomposite: methyl orange adsorption and mechanism studies, *Int. J. Biol. Macromol.* 129 (2019) 98–109.
- [37] B.M. Babić, S.K. Milonjić, M.J. Polovina, B.V. Kaludierović, Point of zero charge and intrinsic equilibrium constants of activated carbon cloth, *Carbon* 37 (3) (1999) 477–481.
- [38] A. De Rossi, L. Simão, M.J. Ribeiro, D. Hotza, R.F.P.M. Moreira, Study of cure conditions effect on the properties of wood biomass fly ash geopolymers, *J. Mater. Res. Technol.* 9 (4) (2020) 7518–7528.
- [39] A.S. El-Shafie, E. Rahman, Y. Gadelhak, R. Mahmoud, M. El-Azazy, Techno-economic assessment of waste mandarin biochar as a green adsorbent for binary dye wastewater effluents of methylene blue and basic fuchsin: lab-and large-scale investigations, *Spectrochim. Acta A Mol. Biomol. Spectrosc.* 306 (2024) 123621.
- [40] K.V.R. Santana, F.C.S.O. Apolônio, A. Wisniewski, Valorization of cattle manure by thermoconversion process in a rotary kiln reactor to produce environmentally friendly products, *Bioenergy Res.* 13 (2) (2020) 605–617.
- [41] J. Jiang, S. Zhang, S. Li, W. Zeng, F. Li, W. Wang, Magnetized manganese-doped watermelon rind biochar as a novel low-cost catalyst for improving oxygen reduction reaction in microbial fuel cells, *Sci. Total Environ.* 802 (2022) 149989.
- [42] O. Pravakar, T. Siddaiah, P.V.R.K. Ramacharyulu, N.O. Gopal, C. Ramu, H. Nagabhushana, Studies on the effect of Cu doping on the structural, thermal and spectroscopic properties of PVA/MAA:EA polyblend films, *Mater. Res. Innov.* 25 (7) (2021) 442–448.
- [43] N.Y. Elamin, A. Modwi, W. Abd El-Fattah, A. Rajeh, Synthesis and structural of Fe₃O₄ magnetic nanoparticles and its effect on the structural optical, and magnetic properties of novel poly(methyl methacrylate)/ polyaniline composite for electromagnetic and optical applications, *Opt. Mater.* 135 (2023) 113323.
- [44] M.A. Irshad, R. Nawaz, M.Z.u. Rehman, M. Adrees, R. Rizwan, S. Ali, S. Ahmad, S. Tasleem, Synthesis, characterization and advanced sustainable applications of titanium dioxide nanoparticles: a review, *Ecotoxicol. Environ. Saf.* 212 (2021) 111978.
- [45] W. Wang, J. Zhang, T. Chen, J. Sun, X. Ma, Y. Wang, J. Wang, Z. Xie, Preparation of TiO₂-modified biochar and its characteristics of photo-catalysis degradation for Enrofloxacin, *Sci. Rep.* 10 (1) (2020) 6588.
- [46] J. Ran, L. Shen, L. Zhong, H. Fu, Synthesis of Silanized MoS₂/reduced graphene oxide for strong radar wave absorption, *Ind. Eng. Chem. Res.* 56 (38) (2017) 10667–10677.
- [47] Y. Liu, L. Wang, X. Dai, J. Zhang, J. Li, Y. Ma, Q. Han, Y. Dong, Research on the adsorption-photocatalytic synergistic degradation of tetracycline by Au nanoparticles/TiO₂ nanorods/biochar, *J. Alloys Compd.* 976 (2024) 172985.
- [48] D. Guo, D. Feng, Y. Zhang, Z. Zhang, J. Wu, Y. Zhao, S. Sun, Synergistic mechanism of biochar-nano TiO₂ adsorption-photocatalytic oxidation of toluene, *Fuel Process. Technol.* 229 (2022) 107200.
- [49] M. El-Azazy, A.S. El-Shafie, K. Al-Saad, Application of Infrared Spectroscopy in the Characterization of Lignocellulosic Biomasses Utilized in Wastewater Treatment, in: M. El-Azazy, K. Al-Saad, A.S. El-Shafie (Eds.), *Infrared Spectroscopy - Perspectives and Applications*, IntechOpen, Rijeka, 2022, <https://doi.org/10.5772/intechopen.108878>, Ch. 8.
- [50] N.J. Castellanos, Z. Martinez Rojas, H.A. Camargo, S. Biswas, G. Granados-Oliveros, Congo red decomposition by photocatalytic formation of hydroxyl radicals (-OH) using titanium metal–organic frameworks, *Transit. Met. Chem.* 44 (1) (2019) 77–87.
- [51] A. Reffas, V. Bernardet, B. David, L. Reinert, M.B. Lehocine, M. Dubois, N. Batisse, L. Duclaux, Carbons prepared from coffee grounds by H₃PO₄ activation: characterization and adsorption of methylene blue and Nylosan red N-2RBL, *J. Hazard. Mater.* 175 (1) (2010) 779–788.
- [52] F.M. Ferraz, Q. Yuan, Organic matter removal from landfill leachate by adsorption using spent coffee grounds activated carbon, *Sustain. Mater. Technol.* 23 (2020) e00141.
- [53] A.U. Nkwoda, G. Onyedika, E. Oguzie, M. Ogwuegbu, Development of PSA@PS-TiO₂ nanocomposite photocatalyst: structure, mechanism, and application using response surface designs and molecular modeling, *Water Sci. Technol.* 87 (11) (2023) 2701–2726.
- [54] S. Mallakpour, E. Nikkhoo, Surface modification of nano-TiO₂ with trimellitylimido-amino acid-based diacids for preventing aggregation of nanoparticles, *Adv. Powder Technol.* 25 (1) (2014) 348–353.
- [55] D. Chen, Y. Cheng, N. Zhou, P. Chen, Y. Wang, K. Li, S. Huo, P. Cheng, P. Peng, R. Zhang, Photocatalytic degradation of organic pollutants using TiO₂-based photocatalysts: A review, *J. Clean. Prod.* 268 (2020) 121725.
- [56] I. Langmuir, The adsorption of gases on plane surfaces of glass, mica and platinum, *J. Am. Chem. Soc.* 40 (9) (1918) 1361–1403.
- [57] M. Temkin, Kinetics of heterogeneous catalysis, *J. Phys. Chem. (USSR)* 14 (1940) 1153–1158.
- [58] H. Freundlich, Über die Adsorption in Lösungen 57U (1) (1907) 385–470.
- [59] M.M. Dubinin, The equation of the characteristic curve of activated charcoal, *Proc. USSR Acad. Sci.* 55 (1947) 327–329.
- [60] W.J. Weber, J.C. Morris, Kinetics of adsorption on carbon from solution, *J. Sanit. Eng. Div.* 89 (2) (1963) 31–59.
- [61] K. Lagergren, S. About the theory of so-called adsorption of soluble substances, *Sven. Vetenskapsakad. Handlingar* 24 (1898) 1–39.
- [62] Y.S. Ho, G. McKay, Pseudo-second order model for sorption processes, *Process Biochem.* 34 (5) (1999) 451–465.
- [63] N.A. Arzaee, N. Betti, A. Al-Amiery, W.N. Roslam Wan Isahak, The role of tin species in doped iron (III) oxide for photocatalytic degradation of methyl orange dye under UV light, *Heliyon* 9(7) (2023) e18076.
- [64] R. Radić, A. Jurov, J. Zavašnik, J. Kovač, V. Brusar, S. Vdović, D. Novko, N. Krstulović, UV and solar-driven photocatalysis of organic dyes using ZnO-ag heterojunction nanoparticles synthesized by one-step laser synthesis in water, *Appl. Surf. Sci.* 669 (2024) 160498.
- [65] R. Thiruganham, A. Kannan, S. Ramasundaram, S. Kumaravel, M. Altaf, T.H. Oh, S. Jayababu, S. Narayanasamy, T. Ganesamoorthy, M. Inbasekaran, Radiant synergy: illuminating methyl orange dye removal with g-C₃N₄/ZnO heterojunction photocatalyst, *Diam. Relat. Mater.* 147 (2024) 111325.
- [66] S. Liang, M. An, S. Xia, B. Zhang, B. Xue, G. Xu, Enhanced photocatalytic degradation of methyl orange by TiO₂/biochar composites under simulated sunlight irradiation, *Opt. Mater.* 142 (2023) 114105.
- [67] B. Li, Z. Zhao, F. Gao, X. Wang, J. Qiu, Mesoporous microspheres composed of carbon-coated TiO₂ nanocrystals with exposed {001} facets for improved visible light photocatalytic activity, *Appl. Catal. B Environ.* 147 (2014) 958–964.
- [68] A. Srihaow, E.E. Win, T. Amornsakchai, T. Kiatsiriroat, P. Kajitvichyanukul, S. M. Smith, Biochar derived from pineapple leaf non-fibrous materials and its adsorption capability for pesticides, *ACS Omega* 8 (29) (2023) 26147–26157.
- [69] S.G. Pouloupoulos, C.J. Philippopoulos, Photo-assisted oxidation of Chlorophenols in aqueous solutions using hydrogen peroxide and titanium dioxide, *J. Environ. Sci. Health A* 39 (6) (2004) 1385–1397.
- [70] R. Ahmad, Z. Ahmad, A.U. Khan, N.R. Mastoi, M. Aslam, J. Kim, Photocatalytic systems as an advanced environmental remediation: recent developments, limitations and new avenues for applications, *Journal of environmental, Chem. Eng.* 4 (4, Part A) (2016) 4143–4164.
- [71] D. Chen, Y. Cheng, N. Zhou, P. Chen, Y. Wang, K. Li, S. Huo, P. Cheng, P. Peng, R. Zhang, L. Wang, H. Liu, Y. Liu, R. Ruan, Photocatalytic degradation of organic pollutants using TiO₂-based photocatalysts: a review, *J. Clean. Prod.* 268 (2020) 121725.

- [72] E. Rápó, S. Tonk, Factors affecting synthetic dye adsorption; desorption studies: a review of results from the last five years (2017–2021), *Molecules* 26 (17) (2021) 5419.
- [73] H. Patel, Elution profile of cationic and anionic adsorbate from exhausted adsorbent using solvent desorption, *Sci. Rep.* 12 (1) (2022) 1665.
- [74] N.R.M. Tanure, L.C. Maia, L.C. Soares, M.M.C. Elias, G.P. da Silva, E.R. de Azevedo, L.V.A. Gurgel, Removal of a model reactive azo dye from aqueous solution by a bioadsorbent in batch and fixed-bed column modes: application of the developed technology to a textile wastewater, *Water Res. Industry* 32 (2024) 100261.
- [75] Y. Lu, J. Chen, Y. Bai, J. Gao, M. Peng, Adsorption properties of methyl orange in water by sheep manure biochar, *Pol. J. Environ. Stud.* 28 (2019) 3791–3797.
- [76] M.A. Hanoon, M.J. Ahmed, Adsorption of methyl orange from wastewater by using biochar, *Iraqi J. Chem. Petrol. Eng.* 20 (3) (2019) 23–29.
- [77] G. Annadurai, R.-S. Juang, D.-J. Lee, Use of cellulose-based wastes for adsorption of dyes from aqueous solutions, *J. Hazard. Mater.* 92 (3) (2002) 263–274.
- [78] C. Diaz-Urbe, J. Ortiz, F. Duran, W. Vallejo, J. Fals, Methyl Orange adsorption on biochar obtained from *Prosopis juliflora* waste: thermodynamic and kinetic study, *ChemEngineering* 7 (6) (2023) 114.
- [79] G.V. Serban, V.I. Iancu, C. Dinu, A. Tenea, N. Vasilache, I. Cristea, M. Niculescu, I. Ionescu, F.L. Chiriac, Removal efficiency and adsorption kinetics of methyl orange from wastewater by commercial activated carbon, *Sustainability* 15 (17) (2023) 12939.
- [80] S. Al-Qaradawi, S.R. Salman, Photocatalytic degradation of methyl orange as a model compound, *J. Photochem. Photobiol. A Chem.* 148 (1–3) (2002) 161–168.
- [81] L. Lu, R. Shan, Y. Shi, S. Wang, H. Yuan, A novel TiO₂/biochar composite catalysts for photocatalytic degradation of methyl orange, *Chemosphere* 222 (2019) 391–398.